Arg-tRNA synthetase links inflammatory metabolism to RNA splicing via nuclear condensates

Haissi Cui[1], Jolene K. Diedrich[1], Douglas C. Wu[2], Justin J. Lim[3,4], Ryan M. Nottingham[2], James J. Moresco[1], John R. Yates III[1], Benjamin J. Blencowe[3,4], Alan M. Lambowitz*[2], Paul Schimmel*[1,5]

[1]Department of Molecular Medicine, The Scripps Research Institute, La Jolla, CA 92037, USA

[2]Institute for Cellular and Molecular Biology and Departments of Molecular Biosciences and Oncology, University of Texas at Austin, TX 78712, USA

[3]The Donnelly Centre, University of Toronto, Toronto, ON M5S 3E1, Canada

[4]Department of Molecular Genetics, University of Toronto, ON M5S 1A8, Canada

[5]Department of Molecular Medicine, The Scripps Research Institute, Jupiter, FL 33458, USA

*Emails: schimmel@scripps.edu, lambowitz@austin.utexas.edu

Summary Cells respond to perturbations such as inflammation by sensing changes in metabolite levels. Especially prominent is arginine, which has long known connections to the inflammatory response. Here we show that depletion of arginine during inflammation decreased levels of arginyl-tRNA synthetase (ArgRS) in the nucleus. We found that nuclear ArgRS interacted with serine/arginine repetitive matrix protein 2 (SRRM2) in membrane-less, condensate-like, SRRM2-dependent nuclear speckles. This interaction impeded SRRM2 speckle trafficking and resulted in changes in alternative mRNA splicing. Splice site usage was regulated in opposite directions by ArgRS and SRRM2. These ArgRS- and SRRM2-dependent splicing changes cumulated in synthesis of different protein isoforms that altered cellular metabolism and peptide presentation to immune cells. Our findings delineate a novel mechanism whereby a tRNA synthetase responds to a metabolic change and modulates the splicing machinery via condensate trafficking for cellular responses to inflammatory injury.

Keywords: aminoacyl-tRNA synthetase, tRNA, nuclear speckle, condensate, multi-synthetase complex, arginine, mRNA processing, inflammation, immune regulation

32 **Introduction**

33 Inflammation is commonly associated with diseases, including cancer, neurodegeneration
34 and auto-immune disorders (Netea et al., 2017). One of the metabolic hallmarks of
35 inflammation is a decrease in systemic arginine levels due to its increased consumption by
36 pro- and anti-inflammatory enzymes, with plasma arginine recovering when the
37 inflammatory insult is resolved (Bronte and Zanovello, 2005; Murray, 2016). Consequently,
38 arginine is a key regulator of cellular signaling pathways, including the central metabolic
39 regulator mTOR, which is necessary for immune cell activation during inflammation (Bar-
40 Peled and Sabatini, 2014; Weichhart et al., 2015; Jones and Pearce, 2017). In addition to
41 its physiological decrease during inflammation, therapeutic arginine depletion by
42 recombinant enzymes is in clinical trials for cancer treatment (Patil et al., 2016).

43 More generally, sensing and responding to external metabolic stimuli are essential for cells.
44 The function of aminoacyl-tRNA synthetases (aaRSs) in cell signal transduction has come
45 into focus in recent years. tRNA synthetases are highly conserved proteins that are essential
46 for mRNA translation, where they catalyze the covalent attachment of amino acids to the 3'
47 end of their cognate tRNAs (Schimmel and Söll, 1979). Eight aaRSs with nine distinct
48 catalytic activities form the multisynthetase complex (MSC) together with 3 designated
49 adapter proteins. While the MSC does not contribute to protein synthesis, complex formation
50 is crucial for the intracellular distribution of aaRSs, specifically for their nuclear localization
51 (Cui et al., 2021). The MSC is dynamic and can act as a reservoir to release aaRSs for
52 extra-translational functions (Lee et al., 2004; Ray et al., 2007; Duchon et al., 2017).

53 aaRSs play a prominent role in mediating extracellular and nuclear cell signaling pathways.
54 Although nuclear-localized aaRSs were historically seen as quality control agents for the

55 correct processing of nascent tRNAs before their export to the cytoplasm (Lund and
56 Dahlberg, 1998; Sarkar et al., 1999), they have also been linked to other functions (Guo and
57 Schimmel, 2013; Shi et al., 2017; Kwon et al., 2019) including mediation of small molecule
58 sensing (Sajish and Schimmel, 2015) and regulation of gene expression (Yannay-Cohen et
59 al., 2009; Shi et al., 2014). In addition to freely diffusing nuclear aaRSs, the MSC is also
60 found in the nucleus (Kaminska et al., 2009; Nathanson and Deutscher, 2000).
61 The cell nucleus is organized by biomolecular condensates, membraneless organelles with
62 the characteristics of phase-separated liquids (Shin and Brangwynne, 2017; Hnisz et al.,
63 2017). Despite their lack of a membrane and constant exchange with the surrounding
64 nucleoplasm, these subnuclear domains display structural integrity (Zhu and Brangwynne,
65 2015). In the nucleus, DNA-sparse interchromatin clusters termed nuclear speckles are
66 condensates that sequester proteins with repetitive sequences of low complexity and high
67 disorder, among them factors necessary for mRNA maturation and mRNA splicing
68 (Galganski et al., 2017; Saitoh et al., 2004; Spector and Lamond, 2011). Polymerases and
69 splicing factors are in steady exchange between condensates and the surrounding
70 nucleoplasm (Guo et al., 2019), raising the possibility that nuclear condensate trafficking
71 regulates their functions.
72 Different protein isoforms can be derived from the same coding sequence by alternative
73 splicing, potentially resulting in different functions (Galarza-Muñoz et al., 2017). Intron
74 retention alternative splicing events can post-transcriptionally regulate mRNA levels by
75 impeding transport to the cytoplasm and increasing RNA degradation (Braunschweig et al.,
76 2014). 20% of cassette exons alternative splicing events (where splice sites are variably
77 recognized leading to an exon being either retained or spliced out) are evolutionarily

78 conserved between human and mouse, suggesting functional consequences (Pan et al.,
79 2004).
80 Nuclear speckles have been suggested to store mRNA maturation factors for mRNA
81 processing at their periphery and/or be hubs for mRNA processing (Chen and Belmont,
82 2019). A series of studies has identified SRRM2 (serine/arginine repetitive matrix protein 2,
83 also known as SRm300, gene name *SRRM2*) as a component of spliceosomal complexes
84 (Blencowe et al., 1998, 2000; Zhang et al., 2017) as well as an integral and essential protein
85 for nuclear speckle formation (Miyagawa et al., 2012; Hu et al., 2019; Ilik et al., 2020). During
86 mRNA splicing, the conserved N-terminal domain of SRRM2 engages with exon sequences
87 close to the exon-junction complex and regulates splice site selection (Gautam et al., 2015;
88 Zhang et al., 2017). In line with its importance, SRRM2 mutations, truncations and
89 misregulation have been identified in developmental disorders (Kaplanis et al., 2020),
90 cancer (Tomsic et al., 2015) and Parkinson's disease (Shehadeh et al., 2010).
91 Given the role of arginine metabolism in inflammation (Bronte and Zanovello, 2005), we
92 initiated our studies of the physiological role of nuclear aaRSs with arginyl-tRNA synthetase
93 (ArgRS, gene name: *RARS*). We discovered a pathway through which cells respond to
94 arginine starvation during inflammation through reduced interaction between ArgRS and
95 SRRM2 in nuclear condensates which results in changes in alternative mRNA splicing.
96 These alternative splicing changes culminated in altered cellular metabolism and peptide
97 presentation to the immune system. This work supports a role distinct from previously known
98 functions of aaRSs and extends the reach of aaRSs to regulation of speckle protein
99 trafficking and alternative mRNA splicing in response to a metabolic signal.
100
101 **Results**

102 **Arginine promotes nuclear localization of arginyl-tRNA synthetase**

103 Previous work showed that ArgRS localizes to the nucleus as part of the MSC (Nathanson
104 and Deutscher, 2000). To begin, we re-investigated the nuclear localization of ArgRS using
105 four model systems: (i) human hepatic carcinoma cell line HepG2, (ii) human embryonic
106 kidney endothelial cell line 293T, (iii) murine embryonic fibroblasts, and (iv) mouse liver. We
107 confirmed nuclear ArgRS in all four samples (Figure 1A, Supplementary Figure S1A). As
108 arginine levels regulate central cellular signaling pathways (Bronte and Zanovello, 2005;
109 Saxton et al., 2016), we tested whether nuclear ArgRS levels were affected by a reduction
110 of extracellular arginine. We starved HEK 293T cells of arginine for 6 h by incubation in
111 arginine-free medium and found a reversible decrease of nuclear ArgRS, while cytoplasmic
112 levels were unchanged (Figure 1B).

113 **Arginine depletion and inflammation reduce nuclear ArgRS *in vivo***

114 Next, we verified the effect of arginine starvation on nuclear ArgRS levels in a more
115 physiological model by reducing systemic arginine in mice by intraperitoneal injection of
116 recombinant murine Arginase-1. Plasma arginine was reduced to 30 - 50% (Supplementary
117 Figure S1B), while nuclear ArgRS in the spleen (mostly from immune cells) of the arginine-
118 depleted mice was reduced to < 40% of PBS controls (Figure 1C, $p = 0.03$).

119 As plasma arginine concentration was known to decrease during inflammation (Murray,
120 2016), we tested whether systemic inflammation in mice would similarly affect nuclear
121 ArgRS levels by using the well-established liver toxin carbon tetrachloride (CCl_4) (Horiguchi
122 et al., 2010). Plasma arginine levels dropped to 50% of vehicle controls (Supplementary
123 Figure S1C) and nuclear ArgRS levels in the spleen were reduced by ~60% (Figure 1D).
124 These findings indicated that a decrease in systemic arginine by itself and as a result of

125 inflammation induced by liver injury decreased nuclear ArgRS levels and focused our
126 attention on the function of nuclear ArgRS (Figure 1E).

127 **The ArgRS interactome contains nuclear proteins**

128 To identify interaction partners of nuclear ArgRS, which could offer clues to its function, we
129 enriched ArgRS from the nuclear fraction of HepG2 cells using ArgRS antibodies and
130 characterized its protein interactome using mass spectrometry (Keilhauer et al., 2015). We
131 used label-free quantification (LFQ) to compare intensities against an antibody isotype
132 control and calculated p-values from three replicates (Supplementary Table S1-4). Proteins
133 with a p-value < 0.05 were listed as significantly enriched (Figure 2A). All MSC proteins,
134 except leucyl-tRNA synthetase (LeuRS, gene name *LARS*), were retrieved from the HepG2
135 nuclear fraction (Figure 2A, orange, Supplementary Table S1), suggesting that LeuRS may
136 be absent or sub-stoichiometric in the nuclear MSC. Aminoacyl tRNA Synthetase Complex
137 Interacting Multifunctional Protein 3 (AIMP3) was enriched but with a p-value > 0.05. Thus,
138 by enriching only for ArgRS, we captured nearly all MSC interactions. This result suggests
139 that the MSC is mostly intact in the nucleus of HepG2 cells but may be in a more dynamic
140 form than in the cytoplasm.

141 Besides MSC components, we found several proteins with predominantly nuclear
142 localization in the interactome of nuclear ArgRS (Figure 2A, yellow). To extend these results
143 and avoid artifacts due to the isolation of nuclei, we repeated the experiment using whole
144 cell lysates. Specific and reproducible binding (p-value < 0.05) to nuclear proteins was
145 confirmed (Figure 2A, Supplementary Table S2), despite ArgRS being a predominantly
146 cytoplasmic protein. Consistent with the known cytoplasmic composition of the MSC

147 (Kaminska et al., 2009), LeuRS was retrieved by ArgRS immunoprecipitation from the whole
148 cell lysates of HepG2 cells (Figure 2A).
149 To test if these interactions are limited to the liver carcinoma cell line HepG2, we used the
150 same approach on human embryonic kidney 293T cells (Figure 2A, Supplementary Table
151 S3). Affinity enrichment of ArgRS retrieved the MSC and several proteins with predominately
152 nuclear localization (Figure 2A, B). Comparison between the ArgRS interactomes in the two
153 cell types showed significant overlap but also distinct binding partners (Supplementary
154 Figure S1D). In contrast, the same experimental procedure in 293T cell lysates with an
155 antibody specific to methionyl-tRNA synthetase (MetRS, gene name *MARS*), which is
156 localized to another subcomplex within the MSC (Kim and Kim, 2020), yielded exclusively
157 MSC proteins as significant interactors (p-value < 0.05, Figure 2A, Supplementary Table S4,
158 Figure 2B, lower right).
159 **ArgRS and SRRM2 interact and colocalize in nuclear speckles**
160 Among the ArgRS binding partners, SRRM2 was highly and reproducibly enriched in both
161 293T and HepG2 cells (Figure 2A, B, upper right and lower left, Supplementary Table S5).
162 We subsequently focused on SRRM2 because of its significance as a part of the
163 spliceosome (Blencowe et al., 2000; Zhang et al., 2017; Bertram et al., 2020) and as an
164 essential component for nuclear speckle formation (Hu et al., 2019; Ilik et al., 2020;
165 Miyagawa et al., 2012). We confirmed the interaction between ArgRS and SRRM2 in both
166 HepG2 and 293T cell lysates by reciprocal co-immunoprecipitation and western blotting
167 (Supplementary Figure S1E, F), while MetRS, another component of the nuclear MSC, was
168 not enriched by SRRM2 pulldown (Supplementary Figure S1G). These findings, together

169 with the lack of SRRM2 enrichment in the MetRS interactome (Figure 2B, lower right),
170 indicated that ArgRS interacts with SRRM2 independently of the MSC (Figure 2C).
171 We next assessed where ArgRS and SRRM2 colocalized in intact cells. To verify that
172 SRRM2 localizes to nuclear speckles, we visualized the speckle marker SC35 (also named
173 SRSF2) using confocal microscopy with an antibody raised against an SC35 peptide.
174 SRRM2 staining showed close to 75% overlap with SC35 in distinct structures in the
175 nucleus, as expected for nuclear speckle proteins (Supplementary Figure S2A,
176 Supplementary Video S1).
177 Immunofluorescence staining of ArgRS localized ArgRS in SRRM2-rich areas (Figure 3A,
178 Supplementary Video S2, Supplementary Figure S2B, C for staining specificity and
179 additional images). ArgRS colocalized with SRRM2 preferentially at the periphery of SRRM2
180 condensates (Figure 3A, Supplementary Video S2) as opposed to SC35, which co-localized
181 with SRRM2 throughout its condensate-like structure (Supplementary Video S1). The
182 Manders overlap coefficient, which denotes the correlation of absolute intensities, was
183 calculated for individual cell nuclei and was on average over 0.6 for SRRM2 in
184 ArgRS/SRRM2 co-staining (Figure 3D), suggesting that SRRM2 consistently colocalized
185 with ArgRS. If the Costes method (Costes et al., 2004) was used for thresholding,
186 colocalization increased to > 0.8 for both ArgRS and SRRM2 in the nucleus (Supplementary
187 Figure S2D). In contrast, colocalization of another nuclear protein, the paraspeckle protein
188 SFPQ, with ArgRS, led to a Manders coefficient of < 0.3 (Supplementary Figure S2E).
189 Arginine starvation significantly decreased the Pearson coefficient, which denotes the
190 correlation of relative intensities, between ArgRS and SRRM2 ($p = 0.01$; Supplementary
191 Figure S2F), in agreement with our finding that nuclear ArgRS levels are decreased by

192 arginine starvation. In accordance with our mass spectrometry results (Figure 2), the
193 Manders coefficient for SRRM2/MetRS colocalization was only 0.13, as opposed to 0.65 for
194 SRRM2/ArgRS (Figure 3B, D, Supplementary Video S3, $p < 0.0001$). If ArgRS interacts with
195 SRRM2 while in the MSC, MetRS would be expected to colocalize with SRRM2 as well
196 (Figure 3B, 3D). The majority of nuclear ArgRS did not colocalize with nuclear MetRS while
197 cytoplasmic ArgRS and MetRS showed high colocalization (Manders coefficients 0.08 vs
198 0.72, Figure 3C, 3D, Supplementary Video S4), suggesting that the majority of nuclear
199 ArgRS is not bound to the MSC. These results point to an ArgRS-specific, MSC-independent
200 association with SRRM2 within or on the periphery of nuclear speckles (Figure 3E).

201 **ArgRS depletion enhances SRRM2 mobility in nuclear speckles**

202 Nuclear speckles contain splicing factors that are in steady exchange with the surrounding
203 nucleoplasm to facilitate splicing (Galganski et al., 2017; Chen and Belmont, 2019). ArgRS
204 co-localized with the core nuclear speckle protein SRRM2 in the periphery of SRRM2-dense
205 signals. We wondered whether ArgRS might thereby influence SRRM2 mobility and
206 trafficking based on the interaction we observed via mass spectrometry, co-
207 immunoprecipitation, and co-localization via microscopy. To address this question, we used
208 fluorescence recovery after photobleaching (FRAP) to monitor SRRM2 flux (Figure 4A). For
209 FRAP measurements, we fluorescently labeled endogenous SRRM2 by introducing an
210 mVenus-tag four amino acids from the C-terminus of SRRM2 (Supplementary Figure S2G).
211 As expected, SRRM2-mVenus in 293T cells localized to nuclear regions in the same distinct
212 pattern as antibody-stained endogenous SRRM2 (Supplementary Figure S2H).

213 For FRAP experiments, regions of interest (ROIs) were chosen that contain one nuclear
214 speckle including its surrounding nucleoplasm (Figure 4A). Bleaching of SRRM2-mVenus in

215 ROIs was followed by a time-dependent recovery of fluorescence that plateaued within 60 s
216 (Supplementary Figure S2I) through influx of SRRM2 from the surrounding SRRM2-rich
217 condensates and nucleoplasm (Figure 4A, Supplementary Video S5-7). About 50% of
218 SRRM2 in the ROIs was immobile (Supplementary Figure S2J). A one-exponential curve fit
219 of background-subtracted, normalized fluorescent recordings estimated a recovery half-time
220 of 17 s in arginine-rich medium (Figure 4B, D). This half-time of recovery is 5x longer than
221 that for the nuclear speckle marker protein ASF/SRSF1 (3 s, Phair and Misteli, 2000). If
222 SRRM2 and SRSF1 have dynamic movements that reflect simple diffusion kinetics, where
223 the rate of diffusion varies inversely with the square root of the molecular weight, then the
224 10-fold higher molecular weight of SRRM2 would predict a 3x difference in their dynamics
225 for spherical objects. From this perspective, given the disordered structure of both proteins,
226 but especially of SRRM2, a 5-fold higher half-time of recovery seems reasonable. Arginine
227 starvation, which decreased the amount of nuclear ArgRS (Figure 1B), increased SRRM2
228 mobility as indicated by the shorter half-time of recovery of SRRM2 (11 s vs 18 s) (Figure
229 4B, Supplementary Figure S2K).
230 The above findings suggested that interaction of ArgRS with SRRM2 in the nucleus
231 decreases SRRM2 mobility. To further investigate this possibility, we stably introduced
232 shRNAs directed against the 3' UTR (shRARS_1) or 5' end (shRARS_2) of *RARS* mRNA.
233 With both shRNAs, we reduced the ArgRS protein level in SRRM2-mVenus-expressing
234 293T cells to ~40% of that in cells expressing a non-targeting shRNA control (Figure 4C).
235 This level of ArgRS knock down did not decrease cell viability or proliferation
236 (Supplementary Figure S2L), in agreement with findings for knock downs of other aminoacyl-
237 tRNA synthetases (Hayano et al., 2016; Ofir-Birin et al., 2013) and in a haplo-insufficient

238 mouse (Seburn et al., 2006). SRRM2 protein expression levels were not reduced by the
239 ArgRS knock downs (Supplementary Figure S2M). In both ArgRS knock down cell lines the
240 half-time of recovery in SRRM2-mVenus regions decreased significantly to ~70% of the
241 control ($p = 0.048$, 0.007) (Figure 4D, Supplementary Video S5-7), consistent with the
242 increased mobility of SRRM2 seen for arginine starvation. Collectively, these findings
243 indicate that the SRRM2-ArgRS interaction slowed SRRM2 speckle-trafficking, and that this
244 interaction is modulated by the external arginine concentration, which in turn controls the
245 amount of ArgRS in the nucleus (Figure 4E).

246 **ArgRS affects processing of mRNAs but not small ncRNAs**

247 As SRRM2 is both a speckle organizer and spliceosome component, we hypothesized that
248 arginine-mediated changes in the level of nuclear ArgRS, which impact SRRM2 exchange
249 between speckles and nucleoplasm, could affect RNA processing. Because manipulation of
250 arginine triggers several cross-talking cellular signaling pathways (Bar-Peled and Sabatini,
251 2014; Dong et al., 2000), we used ArgRS and SRRM2 knock downs as surrogates to assess
252 how changes in SRRM2 mobility due to its interaction with ArgRS might affect gene
253 expression. For this purpose, we stably knocked down ArgRS in HepG2 cells (to ~ 50% on
254 the protein level and ~ 40% on the RNA level, Supplementary Figure S3A, B) and reset the
255 cellular response to arginine by 6 h of arginine starvation followed by 2 h of arginine
256 supplementation. In previous experiments, we lowered total cellular ArgRS by 90% without
257 affecting tRNA aminoacylation or mRNA translation (Cui et al., 2021). Consequently, the
258 milder knock down of ArgRS to 50% was not expected to affect ArgRS' housekeeping
259 function in protein synthesis. We isolated RNA from a control shRNA-expressing cell line

260 (shSCR ctrl) and one expressing a shRNA against ArgRS (shRARS) and confirmed that the
261 knock down did not impair cell proliferation (Supplementary Figure S3C).
262 For a comprehensive view of the effect of ArgRS depletion on cellular RNA synthesis, we
263 used TGIRT-seq of chemically fragmented, rRNA-depleted cellular RNAs. This method
264 employs the novel template-switching activity of the TGIRT enzyme for 3' RNA-seq adapter
265 addition and enables profiling of coding and non-coding RNAs simultaneously (Figure 5A)
266 (Qin et al., 2016; Nottingham et al., 2016; Boivin et al., 2018).
267 Comparing 21,540 different coding and non-coding RNAs showed relatively little difference
268 in the proportion of different RNA biotypes between the ArgRS shRNA knock down and
269 control shRNA (Figure 5B). Most differentially expressed genes were protein-coding genes
270 (Figure 5C, D). The ArgRS knock down also resulted in numerous differences in exon usage
271 for these genes (Supplementary Figure S3D). In contrast, we found only minor differences
272 in the levels of small ncRNAs (Figure 5E-H) with only a small change in the relative
273 abundance of only one tRNA ($tRNA^{Asn}$-GTT-10-1, p-value = 0.01) and no significant changes
274 in the relative abundance of other tRNAs, including $tRNA^{Arg}$ isodecoders (Figure 5H,
275 Supplementary Table S6).

276 **ArgRS knock down alters mRNA processing and protein isoforms**

277 Due to the higher representation of small ncRNAs, the sequencing depth we achieved with
278 TGIRT-seq for mRNA exon-exon junctions was insufficient to draw conclusions about the
279 significance of changes in splice junction usage. Thus, we prepared and sequenced libraries
280 from the same RNA preparations after pre-selection for poly(A)-containing mRNAs. We used
281 vast-tools (Tapial et al., 2017) to evaluate previously annotated splice junctions based on
282 reads spanning exons (in the following referred to as “alternative splicing events”). We first

283 identified alternative splicing events that were affected by ArgRS knock down compared to
284 the shSCR control (Han et al., 2017; Irimia et al., 2014). For this purpose, we used the
285 minimum value of the difference (denoted MV) as a measure of significance, where MV > 0
286 means a ≥ 0.95 probability that splice junction usage changed between the ArgRS knock
287 down and the control (Han et al., 2017) (see Methods). These events were then further
288 classified by |ΔPSI|, which is defined as the % difference spliced-in. We thus identified 393
289 events in 345 genes with alternative splicing changes between the ArgRS knock down and
290 control with MV > 0 (Figure 6A shows events with |ΔPSI| > 0.1, Supplementary Table S7).
291 These alternative splicing events corresponded predominantly to the inclusion or skipping
292 of cassette exons and increased retained introns, while inclusion or skipping of microexons
293 (3-27 nt) or use of alternative 5' or 3' splice sites were relatively unaffected by the ArgRS
294 knock down (Fig. 6A).
295 We also analyzed differential transcript usage with DEXseq (Anders et al., 2012), which
296 compares expression levels of individual exons to the rest of the gene as opposed to
297 quantifying splice junction spanning reads. By using this complementary method, we
298 identified 1,004 exons in 533 genes that were differentially expressed upon ArgRS knock
299 down compared to the control (padj < 0.05, Figure 6B, Supplementary Table S8).
300 By using RT-PCR, we directly confirmed alternative splicing events upon ArgRS knock down
301 for *FGFR3* and *PLEKHG5* in HepG2 cells (Supplementary Figure S4A, B). These genes
302 displayed the same regulation in HEK 293T cells upon ArgRS knock down (Supplementary
303 Figure S4A, B). Rescue of ArgRS knock down by overexpression of a *RARS* transgene
304 restored the ratio of *FGFR3* splice variants to that of control cells (Supplementary Figure
305 S4C, D).

306 To investigate if these splicing changes upon ArgRS knockdown led to an altered proteome,
307 we assessed splice variants using mass spectrometry. As proteins derived from alternative
308 splicing can only be identified from individual peptides (Blencowe, 2017), we sought to
309 increase the sensitivity of detection by enriching these peptides. Therefore, we focused on
310 events where alternative splicing would give rise to distinct N-termini and enriched N-
311 terminal peptides by removing all other (tryptic) peptides (Kleifeld et al., 2011). We identified
312 167 peptides from 135 proteins (Supplementary Table S9) that were detected at higher or
313 lower intensity upon ArgRS knock down (|pdiff| > 1). Ten proteins were encoded by genes
314 with differential exon usage and seven by genes with alternative splicing events upon ArgRS
315 knockdown (Supplementary Figure S4E), including splicing changes that affected peptides
316 in the proximity of potential alternative translation start sites (Supplementary Figure S4F).
317 For the splicing factor PTBP1, we saw an increase of the N-terminal peptide for one isoform
318 while the N-terminal peptide of another isoform was simultaneously reduced
319 (Supplementary Figure S4F). Differences in PTBP1 isoform usage were confirmed by
320 western blots (Supplementary Figure S4G). Collectively, these findings indicate that ArgRS
321 knock down at levels that do not affect cell proliferation results in alternative splicing changes
322 that lead to different protein isoforms.

323 **Identification of SRRM2-dependent splicing changes**

324 Nuclear ArgRS interacts with and impedes SRRM2 mobility in the nucleus (Figure 4) and
325 could thereby reduce the levels of SRRM2 available for RNA splicing. To identify alternative
326 splicing events that are sensitive to decreasing levels of functional SRRM2 and might
327 therefore be regulated by its interaction with ArgRS, we knocked down SRRM2 by 50%
328 (RNA and protein level, Supplementary Figure S5A). This knockdown led to 1,033

329 alternative splicing events in 807 genes with MV > 0 (Figure 6C shows events with |ΔPSI| >
330 0.1, Supplementary Table S10) and 42,140 differential exon usage events in 8,563 genes
331 that were changed relative to the control shRNA (Figure 6D, Supplementary Table S11, padj
332 < 0.05). The numbers of changed alternative splicing and differential exon usage events
333 were much higher than those for the ArgRS knock down (393 and 1,004, respectively)
334 (Figure 6A), as expected for a spliceosome component, whose activity might be subject to
335 multiple modes of regulation. Cassette exons were changed in both directions upon SRRM2
336 knock down while introns were increasingly spliced out (Figure 6C). In order to rule out that
337 the alternative splicing changes were due to off-target effects of the SRRM2 knock down
338 with a single shRNA, we transfected 293T cells with a pool of siRNAs against SRRM2.
339 Alternative splicing of *FGFR3* and *CDK5RAP3* genes could also be observed upon the
340 reduction of SRRM2 with an heterogenous pool of siRNAs, suggesting that this was a direct
341 consequence of lowered SRRM2 availability (Supplementary Figure S5B).

342 **ArgRS and SRRM2 modulate alternative splicing of a set of genes in opposite**
343 **directions**

344 After obtaining lists of genes that were sensitive to reduction of either SRRM2 or ArgRS, we
345 next set out to identify which genes were shared between both and might be regulated by
346 the interaction between ArgRS and SRRM2 described above. To control for indirect effects
347 due to knockdown of an aaRSs, we also knocked down MetRS to 10% on RNA and protein
348 level (which is lower than the ArgRS knock down, Figure S3A) as a control (Supplementary
349 Figure S6A, Supplementary Table S12). We identified 602 alternative spicing events in 493
350 genes (|MV| > 0, events with |ΔPSI| > 0.1 shown in Supplementary Figure S6B) and 50,896

351 differentially expressed exons in 7,668 genes that changed upon MetRS knock down
352 (Supplementary Figure S6B).
353 A total of 282 alternative splicing events overlapped between the ArgRS, SRRM2, and
354 MetRS knock downs (Supplementary Figure S6C, Venn diagram, MV > 0, no criterion for
355 |ΔPSI| to depict all events regardless of magnitude). Of these, 70 splicing events were
356 shared between the SRRM2 and ArgRS knock downs (Supplementary Figure S6C) and their
357 ΔPSIs were negatively correlated (R = -0.29, p = 0.037). We then compared the directionality
358 of the overlapping splicing events between ArgRS and SRRM2 knock downs and identified
359 27 of the 70 shared alternative splicing events (38.6%) that were inversely regulated by
360 ArgRS and SRRM2, meaning that the knock down of ArgRS led to a ΔPSI > 0, while knock
361 down of SRRM2 led to a ΔPSI < 0 or vice versa (Supplementary Figure S6D, inner brown
362 circle, MV > 0, hypergeometric test for overrepresentation p = 0.01). In contrast, only 12/185
363 splicing events (6.2%) were inversely regulated by MetRS and SRRM2 (Supplementary
364 Figure S6D, MV > 0, hypergeometric test p = 1). We confirmed splicing changes by RT-PCR
365 for prominently changed events (*CDK5RAP3*, *IL32, RAD52*, and *STX16*, all Supplementary
366 Figure S6E).
367 If focusing on genes that were alternatively spliced and shared between the ArgRS and
368 SRRM2 knock downs (instead of individual splicing events within a gene that were shared),
369 close to 500 genes had splicing events or differentially expressed exons that were inversely
370 regulated by ArgRS and SRRM2 (72 and 475, respectively, Figure 6E, F). These findings
371 indicate that specific genes are inversely regulated by ArgRS and SRRM2 in their alternative
372 splicing and could lead to different protein isoforms (Figure 6G).
373 **ArgRS and SRRM2-regulated splicing alters cellular metabolism and communication**

374 To explore the possible biological consequences of the ArgRS/SRRM2 interaction, we
375 examined the enrichment of pathways and GO terms in the genes changed in opposite
376 directions in the ArgRS and SRRM2 knock downs (Figure 7A, B, Supplementary Figure S7A-
377 E). Among these were genes that might benefit the cellular response to inflammation such
378 as the pro-inflammatory cytokine IL32 (Supplementary Figure S6E) (Aass et al., 2021).
379 Overrepresented pathways included the mTORC1-pathway, which can be activated by
380 arginine (Figure 7B).
381 To investigate the functional consequences of differential exon usage that might be
382 regulated by the ArgRS/SRRM2 interaction, we chose several mTORC1-associated genes
383 (Supplementary Table S13, Supplementary Figure S7F) and compared the enzymatic
384 activity of their encoded proteins after ArgRS or SRRM2 knock down. The enzyme Isocitrate
385 dehydrogenase 1 (IDH1) responds to cell stress by regulating intracellular NADP/NADPH
386 levels (Itsumi et al., 2015). Differential exon usage in *IDH1* correlated with an increase in
387 IDH enzymatic activity in cell lysates upon SRRM2 knock down while ArgRS knock down
388 led to decreased activity (Figure 7C). Differential exon usage was also found for genes
389 encoding components of the ubiquitin/proteasome system (UPS), including the 19S
390 proteasomal subunit de-ubiquitinating enzyme UCHL5 and the catalytically active
391 proteasomal subunit PSMB5 (β5). These correlated with increased β5 activity upon SRRM2
392 knock down and decreased β5 activity upon ArgRS knock down (Figure 7D).
393 The UPS provides peptides that are presented on the cell surface by the major
394 histocompatibility complex I (MHCI) and alternative splicing of UPS components, such as
395 the β5 proteasomal subunit, could result in differences in peptide processing and
396 consequentially peptides presented to immune cells by MHCI. Additionally, other splicing

397 changes due to ArgRS and SRRM2 knock down that result in different protein isoforms could
398 yield alternative peptides directly through differences in amino acid sequence and alternative
399 protease cleavage sites. These MHCI-bound peptides communicate the status of the
400 presenting cell to immune cells (Rock et al., 2016).
401 To investigate whether communication to immune cells through MHCI might be changed by
402 ArgRS and SRRM2 knock down (Figure 7E), we compared their MHCI-bound peptidome
403 using mass spectrometry. The detected MHCI-bound peptides matched previously
404 described MHCI-bound peptides in length and a preference for the amino acids Tyr and Leu
405 in position 2 (Bassani-Sternberg et al., 2015) (Supplementary Figure S7G). Overall, MHCI
406 protein levels and the spectral counts for the measured peptides were comparable between
407 all treatments (Supplementary Figure S7G, Figure 7F). However, upon sequencing of the
408 peptides presented by MHCI by mass spectrometry, we found that ArgRS knock down
409 substantially reduced the peptide diversity displayed on MHCI (20 vs 104). In contrast,
410 SRRM2 knock down led to the presentation of a comparable number of different peptides
411 by MHCI as the shSCR control (81 vs 104, Figure 7F, see also Supplementary Figure S7H).
412 Nineteen of these peptides were unique for the SRRM2 knock down cell line and 41 were
413 unique for shSCR control, suggesting that SRRM2 knock down led to the presentation of an
414 altered set of MHCI-bound peptides (Figure 7F, Supplementary Figure S7H).
415 In order to predict how these MHCI peptide pools would influence communication with
416 immune cells, we calculated MHCI immunogenicity scores (Figure 7F). A higher score
417 predicts that these peptides would be more likely recognized by T cells and therefore more
418 likely to elicit an immune response (Calis et al., 2013). Consistent with our model, in which
419 ArgRS knock down mimics inflammation, MHCI peptides presented in ArgRS knock down

420 cells had a higher median score than peptides that were exclusively presented by SRRM2
421 knock down cells (Figure 7F). Collectively, these findings support the hypothesis that ArgRS
422 and SRRM2 regulate cellular metabolism and communication to contribute to the cellular
423 response to inflammation (Figure 7G).
424
425 **Discussion**
426 Here we found that a portion of ArgRS localizes to the cell nucleus and that nuclear ArgRS
427 levels fluctuate in an arginine-dependent manner (Figure 1). To characterize the function of
428 ArgRS in the nucleus, we assessed the ArgRS interactome and found that ArgRS interacted
429 with the serine/arginine repetitive matrix protein SRRM2 (Figure 2) and that SRRM2 and
430 ArgRS colocalized to nuclear condensates (Figure 3). We showed that both arginine
431 starvation and depletion of ArgRS increased SRRM2 mobility (Figure 4), suggesting that the
432 nuclear presence of ArgRS impedes SRRM2 trafficking. Upon ArgRS knock down, depletion
433 of nuclear ArgRS and the resulting altered SRRM2 mobility correlated with numerous
434 changes in SRRM2-dependent alternative splicing, while in contrast, small noncoding RNAs
435 were largely unaffected by the ArgRS knock down (Figure 5, 6). We found further that
436 SRRM2 and ArgRS knock downs modulated alternative splicing of a subset of genes in
437 opposite directions, supporting the hypothesis that ArgRS-SRRM2 interaction affects
438 SRRM2's function (Figure 6). Two inversely regulated genes, *IDH1,* which encodes
439 isocitrate dehydrogenase 1, and *PSMB5,* which encodes the β5 subunit of the 20S
440 proteasome, showed that the inversely regulated alternative splicing changes had opposite
441 effects on the biochemical activities of the encoded proteins. These changes in enzymatic
442 activity impacted cellular metabolism and, together with alternative splicing changes in other

443 proteins, led to altered MHCI peptide presentation in a manner consistent with a cellular
444 response to inflammation (Figure 7).
445
446 Arginine levels decrease during inflammation as pro- and anti-inflammatory enzymes
447 compete for arginine as a substrate (Bronte and Zanovello, 2005). Eventually, the depletion
448 of arginine leads to the resolution of inflammation due to a restraining effect on immune
449 cells, especially T cells (Geiger et al., 2016; Murray, 2016). Therefore, the ArgRS/SRRM2
450 interaction and its consequences could have alternative outcomes at different stages of
451 inflammation. Additionally, arginine is a key regulator of the mTOR pathway (Saxton et al.,
452 2016; Wyant et al., 2017), and we found that expression of functionally diverse splice
453 variants of mTORC1 pathway-associated genes (Figure 7B) - driven by the ArgRS/SRRM2
454 interaction - had consequences for multiple functions of that pathway. Because manipulation
455 of arginine triggers several cross-talking cellular signaling pathways (Bar-Peled and
456 Sabatini, 2014; Dong et al., 2000), we focused on using ArgRS knock downs to specifically
457 study ArgRS' relationship with SRRM2. The observed downregulation of IDH1 activity and
458 thereby NADPH production by ArgRS knock down for example would support the metabolic
459 shutdown initiated by mTOR inhibition upon arginine depletion.
460
461 We showed previously that ArgRS' presence in the nucleus is dependent on its presence in
462 the MSC as nuclear ArgRS was strongly reduced upon exclusion of ArgRS from the MSC
463 (Cui et al., 2021). Here, we found that ArgRS – once in the nucleus – interacted with SRRM2
464 independently of the MSC, as affinity enrichment of ArgRS, but not MetRS, another
465 component of the MSC, retrieved SRRM2 (Figure 2B, lower right). These finding suggest

466 that in addition to tRNA quality control (Lund and Dahlberg, 1998), the nuclear MSC might
467 act as a reservoir of nuclear aaRSs with regulatory functions that are sequestered until a
468 cue induces their release. This concept is similar to that suggested for the cytoplasmic MSC
469 (Ray et al., 2007). Operationally, this function of the MSC resembles that of nuclear
470 speckles, where highly disordered, low complexity proteins are sequestered (Galganski et
471 al., 2017). We hypothesize that both the MSC and nuclear speckles are dynamic reservoirs
472 in steady exchange with their surroundings that enable the correct localization and the
473 controlled release of their components. ArgRS, with changing arginine levels as a cue, thus
474 connects two distinct protein organizational structures with central roles in transcription and
475 translation. Due to their ability to sense and respond to changes in amino acids levels and
476 interact with a variety of other proteins, aaRSs are uniquely poised to function in metabolite
477 sensing and signal transduction (Netzer et al., 2009; Sajish and Schimmel, 2015; Son et al.,
478 2019).
479
480 ArgRS and SRRM2 colocalized more towards the interface between nuclear speckles and
481 nucleoplasm as compared to SRRM2 and SC35, another speckle marker (Supplementary
482 Video S1, S2). mRNA processing and transcription have been shown to take place at or in
483 close proximity to nuclear speckles (Chen and Belmont, 2019). A recent model suggested
484 that splice site selection is regulated by partial immersion of unspliced pre-mRNAs in
485 condensates at the interface between nuclear speckles and nucleoplasm (Liao and Regev,
486 2021). The interaction between ArgRS and SRRM2 could therefore impact alternative
487 mRNA splicing directly by disrupting SRRM2's function within the spliceosome and/or by
488 regulating trafficking of SRRM2 to the nuclear speckle-nucleoplasm interface.

489

490 SRRM2 is essential for nuclear speckle formation (Ilik et al., 2020) and simultaneously a
491 component of active spliceosomes (Bertram et al., 2020). The N-terminal 1% of SRRM2 is
492 immobilized sufficiently in the spliceosome to be resolved by cryo-EM while the remaining
493 99% is disordered (Bertram et al., 2020). SRRM2 would therefore be an ideal candidate to
494 anchor spliceosomes to the nuclear speckle interface. Due to its large size and many
495 phosphorylation sites, SRRM2 provides ample interaction surface for other splicing
496 regulatory proteins to gather in the proximity of the spliceosome and in nuclear speckles.
497 Our results suggest that these functions of SRRM2, which are dependent on its constant
498 trafficking, could be impeded by SRRM2 sequestration by ArgRS (Figure 3).

499

500 A previous study in a murine liver cell line, in which SRRM2 was more severely depleted
501 than in our study, found that immune response genes were upregulated in their expression
502 and mRNA splicing (Hu et al., 2019). Here, we show that modulation of SRRM2 levels
503 impacted cellular metabolism and MCHI peptide processing (Figure 7). MHCI presentation
504 allows cells to communicate with the immune system (Rock et al., 2016). In pathological
505 scenarios, such as viral infection and cancer, an altered MHCI peptidome could induce a
506 different immune response. We found that ArgRS knock down, which mimics arginine
507 starvation by leading to decreased concentrations of ArgRS in the nucleus, led to a decrease
508 in peptide diversity without reducing the total amount of detectable MHCI-presented
509 peptides (Figure 7F). These peptides were also predicted to be more immunogenic (Figure
510 7F) and might therefore be preferentially recognized for example by cytotoxic T cells during
511 cancer and viral infections, in which inflammation is induced. During inflammatory

512 conditions, the reduction of peptide diversity and increase in immunogenicity presented by
513 MHCI upon ArgRS knock down could enable more efficient identification by the immune
514 system. On the other hand, SRRM2 knock down led to the presentation of a different set of
515 MHCI peptides as compared to control (Figure 7F), suggesting that sequestration of SRRM2
516 by ArgRS could potentially increase the diversity of MHCI peptide presentation. Those MHCI
517 peptides exclusively found on SRRM2 knock down cells were predicted to be less
518 immunogenic (Figure 7F). Recently, splicing inhibitors have been used to modulate the
519 MHCI peptidome to increase sensitivity to immune therapy in cancer (Lu et al., 2021) and
520 our findings suggest that a comparable mechanism to modulate and diversify MHCI peptide
521 variety is employed during inflammation. Therefore, the interplay of arginine, ArgRS, and
522 SRRM2 would enable cells to not only detect ongoing extracellular inflammation by picking
523 up metabolic cues but also by responding adequately by adapting their proteome and tuning
524 the communication with immune cells during inflammation.
525
526

527 **Data availability**

528 TGIRT-seq data are deposited in the NCBI sequence read archive and accessible through
529 the BioProject number PRJNA561913. Poly(A) RNA-seq data are deposited GEO
530 GSE165513. Mass spectrometry data is deposited on ProteomeXchange Consortium via
531 the PRIDE partner repository with the dataset identifiers PXD015692 (interactomes),
532 PXD024091 (N-terminomics), and PXD027531 (MHCI peptidome).

533

534 **Acknowledgements**

535 We thank the Center for Metabolomics, the Microscopy core, the High Performance
536 Computing team, and Flow Cytometry Core, all at Scripps Research, for training and
537 instrument maintenance, and the staff at the Genomic Sequencing and Analysis Facility at
538 the University of Texas at Austin for poly(A) library preparation and sequencing. Access to
539 a plate reader and flow cytometry software was provided by Prof. James Paulson and
540 access to a ChemiDoc Imager by Prof. Jeffrey Kelly, both at Scripps Research. We thank
541 Aditi Dutta for preliminary analysis of ArgRS- and MetRS-dependent signaling pathways.
542 We also thank Dr. Ulrich Braunschweig, Dr. Rasim Barutcu, and Mingkun Wu (all University
543 of Toronto) for feedback on the experimental design (UB) and the manuscript (RB, MW). We
544 thank Professors David Sabatini, Phillip A. Sharp, and Landon J. Edgar for reading the
545 manuscript and their insightful comments. This work was supported by the National
546 Foundation for Cancer Research to PS, the DFG (327097878) and the HFSP (LT000207)
547 to HC, NIH grant P41 GM103533 to JRY, NIH grant R35 GM136216 and Welch Foundation
548 grant F-1607 to AML, and a CIHR Foundation Grant to BJB.

549

550 **Author contributions**

551 HC planned and conducted experiments and analyzed data. JKD, JJM, and JRY performed,
552 analyzed, or supervised mass spectrometry experiments. DCW, RMN, and AML performed,
553 analyzed, or supervised TGIRT-seq and RNA-seq library preparation and sequencing. JJL
554 and BB analyzed RNA-seq results. PS, AML, and HC designed research and wrote the
555 manuscript with input and contributions from all authors.

556 **Corresponding authors**

557 Correspondence to Alan M. Lambowitz (lambowitz@austin.utexas.edu) and Paul Schimmel
558 (schimmel@scripps.edu).

559

560 **Declaration of Interests**

561 Thermostable Group II Intron Reverse Transcriptase (TGIRT) enzymes and methods for
562 their use are the subject of patents and patent applications that have been licensed by the
563 University of Texas and East Tennessee State University to InGex, LLC. AML and the
564 University of Texas are minority equity holders in InGex, and AML, some members of AML's
565 laboratory, and the University of Texas receive royalty payments from the sale of TGIRT
566 enzymes and the licensing of intellectual property by InGex to other companies.

567

568 **Figure legends**

569 **Figure 1: Arginyl-tRNA synthetase (ArgRS) localized to the nucleus in response to**
570 **external arginine levels.** (A) ArgRS in the cytoplasmic and nuclear fractions of human
571 hepatocellular carcinoma HepG2 or human embryonic kidney (HEK) 293T cells. (B) ArgRS
572 in the nucleus (left) and cytoplasm (right) following cell fractionation. Nuclear ArgRS could

573 be restored by addition of external arginine (0x/10x). Arginine concentrations are relative to
574 DMEM. p = *0.02. (C) Injection of recombinant Arginase-1 reduced nuclear ArgRS in the
575 spleen of mice. p = *0.03. (D) Systemic inflammation by CCl_4 reduced nuclear ArgRS in the
576 spleen of mice. (A-D) Western blots and densitometric quantification. GAPDH: cytoplasmic
577 marker, Tubulin: cytoplasmic marker, Histone H3: nuclear marker. (E) Scheme: Reduction
578 of arginine during inflammation leads to reduced nuclear ArgRS.

579 **Figure 2: Characterization of the ArgRS interactome revealed nuclear proteins as**
580 **interaction partners.** (A) Comparison between the ArgRS interactome in nucleus, HepG2
581 whole cell lysate, 293T whole cell lysate, and with the interactome of MetRS, another tRNA
582 synthetase. Multisynthetase complex (MSC) components: orange. Nuclear proteins: yellow.
583 Proteins are identified by gene names and listed in order of enrichment over a non-targeted
584 antibody of the same isotype with fold-change noted in parentheses. (B) Volcano plots of
585 ArgRS or MetRS interactomes. MSC proteins are highlighted by larger symbol size. Axes
586 denote enrichment (Welch's t-test enrichment, x-axis) and reproducibility between 3 repeats
587 (Welch's t-test significance, y-axis). Color: number of unique peptides detected. Line: p-
588 value = 0.05 (C) Scheme: The MSC is intact in the nucleus and ArgRS interacts with SRRM2
589 independent of the MSC.

590 **Figure 3: SRRM2 colocalized with ArgRS but not with MetRS.** (A-C) Confocal
591 microscopy following immunofluorescent staining of ArgRS/SRRM2 (A), MetRS/SRRM2 (B),
592 or ArgRS/MetRS (C), respectively. A single slice of a series of z-stacks is shown.
593 Colocalized areas in yellow. Bar: A, B: 2 μm. C: 5 μm. (D) Manders coefficients
594 corresponding to panels A-C. Hoechst staining was used to identify the cell nucleus.
595 Manders coefficient was calculated for individual cell nuclei (A, B, n = 11, 12) or for an

596 average for 2-3 cells (C, n = 8). (E) Scheme: ArgRS leaves the multisynthetase complex in
597 the nucleus to interact with SRRM2 in the proximity of nuclear speckles.

598 **Figure 4: ArgRS knock down increased SRRM2 mobility.** (A) Fluorescence recovery
599 after photobleaching (FRAP). SRRM2-mVenus-dense areas were bleached, and recovery
600 was monitored over 90 s. SRRM2-mVenus is displayed as a 16-color lookup table with white
601 and red indicating the highest intensity and blue and green the lowest. (B) Arginine starvation
602 reduced SRRM2-mVenus FRAP half-time $t_{1/2}$ to 60% as compared to high arginine. Arginine
603 concentrations relative to DMEM, n = 8, p = **0.001. (C) Stable knock down of ArgRS in
604 SRRM2-mVenus cell lines with two different shRNAs (shRARS_1, shRARS_2) reduced
605 ArgRS protein levels to 40% of a non-targeting shRNA control, shown by western blot.
606 Relative *RARS* mRNA levels quantified by qRT-PCR: shSCR: 1.00 ± 0.17; shRARS_1: 0.20
607 ± 0.17; shRARS_2: 0.07 ± 0.06. (D) Left panel: Recovery of fluorescent signal after
608 photobleaching. Errors bars depict standard error of the mean. Right panel: $t_{1/2}$ of SRRM2-
609 mVenus recovery time after bleaching was reduced to 70% by stable ArgRS knock down.
610 shSCR: n = 10, shRARS_1: n = 11, shRARS_2: n = 12, p = *0.048, **0.007. (E) Scheme:
611 ArgRS impedes SRRM2 trafficking by slowing the exchange between condensates and
612 nucleoplasm.

613 **Figure 5: ArgRS knock down primarily affected mRNAs but not non-coding RNAs.** (A)
614 Stacked bar graphs showing RNA biotype distributions. (B) Scatter plot comparing RNAs. ρ
615 is the Spearman's correlation coefficient. (C-H) Volcano plots comparing all and different
616 RNA biotypes in ArgRS knock down versus control HepG2 cells. Vertical dashed lines depict
617 a 1.5-fold change and horizontal dashed line a padj < 0.05. Differential expression of (C) all
618 RNAs, (D) mRNAs, (E) small non-coding RNAs, (F) microRNAs, (G) small nucleolar RNAs,

619 and (H) transfer RNAs. (A-H): ctrl: HepG2 shSCR control. shRARS: HepG2 ArgRS knock
620 down. Three replicate TGIRT-seq datasets.

621 **Figure 6: Differential mRNA processing upon ArgRS knock down.** (A) Splicing event
622 changes upon ArgRS knock down (shRARS). (B) Volcano plot of differentially expressed
623 exons upon ArgRS knock down (shRARS). (C) Splicing event changes upon SRRM2 knock
624 down. (D) Volcano plot of differential exon usage upon SRRM2 knock down. (A, C): Splicing
625 events divided by event type, relative to shSCR control, as detected by RNA-seq. Events
626 with a |ΔPSI| > 0.1, MV > 0 are shown. Increased event frequency shown in cyan, events
627 with decreased frequency in pink. PSI: percent spliced in. MV > 0: significant splicing
628 changes. Cassette: cassette exons/exon skipping, microexons: 3-15 nucleotide exons, alt
629 3': alternative 3' end splice site, alt 5': alternative 5' end splice site, intron: intron retention.
630 115814 (shRARS) and 111346 (shSRRM2) events were detected in total. (B, D) Dashed
631 vertical lines: 2-fold change, dashed horizontal line: p-value 1e-6. (E, F) Venn diagram of
632 genes with shared alternative splicing events or differentially expressed exons upon ArgRS
633 and SRRM2 knock down. Genes with inversely regulated (E) splicing events (ΔPSI > 0 for
634 shRARS and ΔPSI < 0 for shSRRM2 or vice versa) or (F) differentially expressed exons
635 (log2fold change > 0 for shRARS or < 0 for shSRRM2 or vice versa) in brown circle.
636 Hypergeometric test for enrichment of inversely correlated, ArgRS regulated splicing events.
637 (A-F) Data was derived from sequencing of 3 replicates. All changes relative to shSCR
638 control. (G) ArgRS slows down SRRM2 trafficking and thereby disrupts SRRM2-dependent
639 mRNA splicing changes, leading to the regulation of alternative mRNA splicing in opposite
640 directions by ArgRS and SRRM2.

641 **Figure 7: SRRM2- and ArgRS-regulated mRNA processing led to metabolic changes**
642 **and an altered MHCI peptidome.** (A) MSigDB and Gene Ontology (GO) analysis of genes
643 with inversely regulated splicing events upon ArgRS and SRRM2 knock down. (B) MSigDB
644 and GO analysis of genes with inversely regulated differentially expressed exons upon
645 ArgRS and SRRM2 knock down. (A, B) GO terms associated with RNA-interacting proteins
646 in fuchsia, GO terms associated with cellular organization and organelles in blue. (C) IDH1
647 enzyme activity. IDH activity assay: representative of 3 repeats, 12 technical replicates, p <
648 ****0.0001. (D) PSMB5 differential exon usage, β5 proteasomal subunit (PSMB5 protein)
649 activity. Quantification of differentially used exon: β5 activity: representative of 3 repeats, 4
650 replicates, p = **0.006, p < ****0.0001. (E) Model of ArgRS and SRRM2 knock down, their
651 connection to inflammation, and consequences on their splice targets. (F) Total spectral
652 counts (upper left) correspond to peptide quantity. Venn diagrams of identified MHCI
653 peptides by mass spectrometry following isolation of MHCI complex (upper right) found in
654 all replicates upon ArgRS or SRRM2 knock down. Bottom: Violin plot of MHCI
655 immunogenicity score for peptides found in all samples, shSCR ctrl, ArgRS knock down,
656 and SRRM2 knock down only. Median MHCI immunogenicity score is indicated by a black
657 line. (A-F) shSCR ctrl: HepG2 shSCR control. shRARS: HepG2 ArgRS knock down.
658 shSRRM2: HepG2 shSRRM2 knock down. (G) Model of cellular response to inflammation
659 by arginine/ArgRS/SRRM2.
660
661

662 **Material and Methods**

663 Further information and requests for resources and reagents should be directed to and will
664 be fulfilled by Prof. Paul Schimmel (schimmel@scripps.edu).

665 **Materials Availability**

666 All unique reagents generated in this study are available from Prof. Paul Schimmel, with a
667 completed Materials Transfer Agreement.

668

669 **Data and Code Availability**

670 TGIRT-seq data are deposited in the NCBI sequence read archive and accessible through
671 the BioProject number PRJNA561913. Poly(A) RNA-seq data are deposited at GEO
672 (GSE165513). Mass spectrometry search results and raw data are deposited in the PRIDE
673 archive as PXD015692 (interactomes), PXD024091 (N-terminomics), and PXD027531
674 (MHCI peptidome).

675

676 **EXPERIMENTAL MODEL AND SUBJECT DETAILS**

677 **Mouse model**

678 6-8-week-old, female C57BL6/J mice from the Scripps Research breeding facility were used.
679 Animals with the same birthdate were randomly assigned to experimental groups. All
680 animals were sacrificed in accordance with animal protocol 19-0023 which was approved by
681 the Scripps Research IACUC Department. Staff and researchers were wearing scrubs,
682 facemasks, and gloves while handling animals. The rooms were kept between 69-78
683 degrees Fahrenheit. Individually ventilated rack caging system consisted of a cage bottom,
684 wire bar lid, and filter top, which were sanitized in a cage wash. Feed was commercially

685 available laboratory grade rodent diet. Purified water through reverse osmosis was provided
686 through an automatic watering system. Cages were changed approximately every 10-14
687 days. Groups consisted of mice injected with (I) 100 µl 35 mg/ml murine Arginase, (II) 100
688 µl PBS control, (III) 50 µl 20% CCl4 in olive oil, or (IV) 50 µl olive oil.

689 **Cell lines**

690 HepG2 human hepatocellular carcinoma cells and human embryonic kidney (HEK) 293T
691 cells were cultured in high glucose DMEM (Gibco) supplemented with 10% fetal bovine
692 serum (FBS, Omega Scientific) and penicillin/streptomycin (Gibco). Both cell lines were
693 regularly tested for mycoplasma contamination with a PCR-based, in-house assay and were
694 consistently negative. HepG2 and 293T cells were verified by the ATCC Cell Line
695 Authentication service using STR Profiling Results. Both cell lines were found to be a 93%
696 match with the reference cell line profile. HepG2 cells were originally derived from a male
697 donor and HEK 293T cells from a female embryo. Murine embryonic fibroblasts (MEF) cells
698 were a kind gift from Yao Tong (Scripps Research). MEFs were generated from C57Bl/6J
699 embryos around E13.5 and used at cell passage 3. The sex of the embryos that were used
700 for MEF generation was not determined.

701 **Statistics**

702 Student's t-test was used to determine significance between groups, except for mass
703 spectrometry data for which Welch's t-test was used. Repeats are different cell passages if
704 not noted otherwise. For densitometric analysis, paired t-test were used as repeats were run
705 on individual gels. GraphPad Prism 8 was used for testing except for large datasets.
706 Significance in large datasets was determined with Perseus for mass spectrometry results,
707 DESeq2 in TGIRT-seq and RNA-seq, DEXSeq in exon analysis, and Vast-Tools in splice

708 junction usage. Correlation coefficients were calculated with Kendall Rank correlation or
709 Pearson correlation and enrichment of gene sets by hypergeometric testing, both in R. If not
710 stated otherwise, significance was defined as * $p < 0.05$, ** $p < 0.01$, *** $p < 0.001$.

711 **Arginine depletion in mice**

712 To enzymatically deplete systemic arginine, mice were i.p. injected with 35 mg/kg
713 recombinant, LPS-free (6.15 EU/mg) murine Arginase-1 purified from Clear *E. coli* (Lucigen)
714 and sacrificed 5-7 hours later. Arginase-1 activity was tested by measuring conversion of
715 arginine to urea. Purified Arginase-1 was mixed with a reaction buffer containing 320 mM
716 arginine, 100 mM Hepes pH 8.5, and 10 mM $CoCl_2$. The reaction was incubated for 45 min
717 at 37°C in a thermocycler. Urea was detected by a colorimetric assay monitoring the
718 conversion of α-Isonitrosopropiophenone. α-Isonitrosopropiophenone was dissolved in
719 ethanol (2 g/50 ml) and freshly diluted 1:10 in 1:1:3 water:sulphuric acid:phosphoric acid to
720 make urea detection reagent. Urea detection reagent was mixed with the Arginase-1
721 reaction product or a urea standard 5:1 and incubated in a thermocycler for 60 min at 100°C
722 followed by 15 min at 25°C.

723 CCl_4 (Sigma Aldrich) was used to elicit systemic inflammation. Mice were i.p. injected with
724 50 µl 20% CCl4 in olive oil, or olive oil only, and sacrificed 30 h later. In all experiments,
725 blood was collected from the inferior vena cava with EDTA-coated syringes and plasma was
726 separated by centrifugation at 500 x g for 3 minutes at 4°C.

727 **Arginine determination in plasma**

728 5 µl 250 µM $13C_6$-arginine (Pierce) was spiked in 20 µl plasma as an internal control. Plasma
729 was precipitated with 200 µl 80% ice-cold methanol and dried in a speedvac. Metabolites
730 were resuspended in 40 µl water and incubated with 20 µl freshly-made 1% Marfey's reagent

731 in acetone (w/v) and 4 µl 1 M sodium bicarb for 1 h at 40°C in a thermocycler. Derivatized
732 amino acids were dried in a speedvac and resuspended in 40 µl 40% methanol. Samples
733 were measured in the Scripps Research open access mass spectrometry core using an
734 Agilent 6125 single quadrupole mass spectrometer coupled to an Agilent 1260 LC stack.
735 The column used was an Agilent SB-C8 5 µm 300 A 4.6x50 mm running at a flowrate of 0.5
736 ml/min. Mobile phases consisted of A (H2O/0.1% formic acid) and B (ACN/0.1% formic acid).
737 Spray chamber conditions were dry gas flowrate = 12 L/min at 350 C, nebulizer pressure =
738 35 psi and capillary voltage = 4000 V for pos mode, and 3500 V for neg mode. 20 µl sample
739 were injected and eluted with a 15 ml 10-35% A to B gradient. Derivatized arginine eluted at
740 9.3 ml. Spectra were collected in a mass range of 150-600 for both positive and negative
741 mode and additionally in the 420-430 Da and 430-440 Da range.

742 **Modulation of arginine levels**

743 For the modulation of arginine in tissue culture, SILAC DMEM with dialyzed FBS and
744 substituted with lysine was used as a base medium. Arginine concentrations are given as
745 relative to 1x DMEM (0.084 g/l L-arginine monohydrochloride, dissolved in PBS). For 0x,
746 arginine concentrations were under the detection limit of the assay described above. Cells
747 were deprived of arginine for 4-6 hours and arginine was added back at the indicated
748 concentrations for 2 h.

749 **Cell fractionation**

750 Cultured cells were seeded at a density of 5 x 10^6 cells per 10 cm tissue culture dish the day
751 before (293T, MEF) or at 2.5 x 10^6 per 10 cm tissue culture dish two days prior (HepG2) to
752 harvest in 500 µL cell fractionation buffer (20 mM HEPES, pH 7.5, 10 mM KCl, 2 mM $MgCl_2$,
753 2 mM EDTA, 1 mM dithiothreitol (DTT), protease inhibitor). Spleens of arginine-depleted or

754 control mice were homogenized by passing through a 40 µm cell sieve. Mouse liver was
755 harvested from 4-week old C57Bl/6J mice and homogenized using a 40 µm cell sieve. The
756 cell suspension was left on ice for 20 minutes for osmotic lysis and 100 µL were taken as
757 whole cell lysate. The remaining cells were passed 10 times through a 27-gauge needle.
758 Nuclei and cytoplasm were separated by centrifugation at 750x g for 5 minutes. The
759 supernatant was taken as cytoplasmic fraction and the nuclear pellet washed three times
760 with cell fractionation buffer. 10x RIPA buffer (0.5 M Tris/HCl, pH 7.4, 1.5 M NaCl, 2.5%
761 Deoxycholate, 10% IGE-PAL CA-630, 10 mM EDTA) was added to 2x final concentration to
762 all fractions. Complete lysis was achieved by freezing and thawing. Lysates were spun down
763 at 14,000x g for 20 min to remove insoluble components and SDS loading buffer was added
764 before western blot analysis.

765 **Affinity enrichment/co-immunoprecipitation**

766 Two days prior to the experiment, $1x10^7$ 293T or $5x10^6$ HepG2 cells were seeded on a 15
767 cm tissue culture dish. Cells were lysed for 20 minutes under mild conditions in 1% IGE-PAL
768 CA-630 (Sigma Aldrich) in Tris-buffered saline (TBS) with protease (Pierce Protein Biology)
769 and phosphatase inhibitors (Pierce Protein Biology). Insoluble components were pelleted by
770 centrifugation at 14,000x g for 20 minutes. Protein A/G agarose beads (30 µL, Santa Cruz
771 Biotechnology) were equilibrated in TBS. Cell lysate was added to the beads together with
772 2 µL antibody against ArgRS (Biorbyt). For immunoprecipitation of SRRM2, antibody against
773 SRRM2 (Santa Cruz Biotechnology) was conjugated to beads using the Co-
774 Immunoprecipitation kit (Pierce Protein Biology) according to the manufacturer's
775 instructions. Immunoprecipitation was performed for 3 h (ArgRS) or overnight (SRRM2).
776 After incubation, the beads were washed twice with TBS containing 0.1% IGE-PAL CA-630

777 and twice with TBS only. Precipitated proteins were either eluted using 0.1 M glycine, pH 3,
778 for western blot or by tryptic digestion for interactome analysis.

779 **Western blot**

780 Cell lysate from different cellular fractions or immunoprecipitated proteins were run on a 4-
781 15% gradient gel (Bolt, ThermoFisher Scientific) and subsequently blotted on a PVDF
782 membrane using an iBlot or iBlot2 device (ThermoFisher Scientific). Membranes were
783 blocked for at least one hour with 5% bovine serum albumin (BSA) or 1% dry milk in TBS-
784 T. Primary antibody was incubated overnight at 4°C at a 1:5000 (ArgRS: Biorbyt, GAPDH,
785 Tubulin, and Histone H3: Cell Signaling Technology, MetRS: Abcam, GFP, PTBP1:
786 Proteintech Group) or a 1:100 (SRRM2, Santa Cruz Biotechnology) dilution in 5% BSA/TBS-
787 T. The next day, blots were washed three times for at least 10 minutes per wash in TBS-T
788 and HRP-labeled secondary antibody (Invitrogen) was added at a 1:10,000 (anti-rabbit) or
789 1:5000 (anti-mouse) dilution in BSA/TBS-T or milk/TBS-T for at least 90 minutes. After three
790 additional washes, membranes were developed with ProSignal Dura ECl (Genesee
791 Scientific) and imaged with a FluorChem M (Proteinsimple).

792 **ArgRS interactome**

793 Proteomes were eluted by incubation with 25 µL 2 M urea, 5 ng/µL trypsin (Pierce Protein
794 Biology), 1 mM DTT in 50 mM Tris/HCl, pH 7.5. After 30 minutes at room temperature, 5 mM
795 chloroacetamide (Sigma Aldrich) was added for alkylation of cysteine residues to a total
796 volume of 125 µL. Samples were digested overnight at 37°C and quenched with 0.5%
797 trifluoroacetic acid (Sigma Aldrich) the next morning. Stage tip desalting was done using
798 C18 spin tips with a 100 µL bed (Pierce Protein Biology) according to the manufacturer's
799 instructions. The digested samples were analyzed on a Q Exactive mass spectrometer

800 (Thermo). Approximately 250 ng of digest was injected directly onto a 20 cm, 100 µm ID
801 column packed with Aqua 3 µm C18 resin (Phenomenex). Samples were separated at a
802 flow rate of 400 nl/min on an Easy nLCII (Thermo). Buffer A and B were 0.1% formic acid in
803 5% acetonitrile and 0.1% formic acid in 80% acetonitrile, respectively. A gradient of 1-35%
804 B over 80 minutes, an increase to 80% B over 25 minutes and held at 80% B for 5 minutes
805 prior to returning to 1% B was used for 120 minutes total run time. Column was re-
806 equilibrated with buffer A prior to the injection of sample. Peptides were eluted directly from
807 the tip of the column and nanosprayed directly into the mass spectrometer by application of
808 2.5 kV voltage at the back of the column. The Q Exactive was operated in a data dependent
809 mode. Full MS^1 scans were collected in the Orbitrap at 70 K resolution with a mass range of
810 400 to 1800 m/z. The 10 most abundant ions per cycle were selected for MS/MS and
811 dynamic exclusion was used with exclusion duration of 15 seconds.
812 Three biological replicates were measured sequentially. Mass spectrometry data was
813 processed with MaxQuant 1.5.7.0 (Cox and Mann, 2008) and Perseus 1.6.2.3 (Tyanova et
814 al., 2016) as described previously (Keilhauer et al., 2015) to identify ArgRS interaction
815 partners. In brief, raw files were searched against *Homo sapiens* reference proteome
816 UP000005640_9606 (UniProt Consortium, 2019) (Uniprot) with the Andromeda search
817 engine integrated in MaxQuant. Default settings were used for label-free quantification
818 (LFQ). Phosphorylated peptides (STY) were included when searching for nuclear interaction
819 partners of ArgRS. The resulting protein groups file was loaded into Perseus and filtered for
820 “reverse”, “potential contaminants”, and “only identified by site”. The log2 values of LFQ
821 intensities were calculated and all proteins with less than two valid values/group discarded.

822 Missing values were replaced from a normal distribution (width 0.3, downshift 1.8) and
823 Welch's t-test was used to calculate t-test significance and difference.

824 **Generation of SRRM2-mVenus cell line**

825 A gRNA (CCAUGAGACACCGCUCCUCC) targeted to the second last exon of SRRM2
826 (exon 14) was inserted into pSpCas9(BB)-2A-GFP. pSpCas9(BB)-2A-GFP (PX458) was a
827 gift from Feng Zhang, Addgene plasmid #48138; http://n2t.net/addgene:48138;
828 RRID:Addgene_48138 (Ran et al., 2013)). mVenus (mVenus C1) was a gift from Steven
829 Vogel, Addgene plasmid #27794; http://n2t.net/addgene:27794; RRID:Addgene_27794
830 (Koushik et al., 2006). The donor vector for insertion of mVenus was based on pcDNA6. The
831 CMV promoter and multiple cloning site of pcDNA6 were substituted for mVenus flanked by
832 800 bp upstream and downstream of the Cas9 cleavage site. Cells were transfected with
833 both plasmids at a 1:2 ratio gRNA/Cas9:donor vector and sorted for GFP expression after
834 two days (successful expression of pSpCas9-GFP) by the Flow Cytometry core at Scripps
835 Research. Single cells were expanded into monoclonal cell lines and evaluated for mVenus
836 expression after expansion by flow cytometry. About 1/3 of all tested clones showed mVenus
837 fluorescence. Correct genomic integration was assessed by PCR on isolated genomic DNA
838 (DNeasy Blood and Tissue Kit, Qiagen, Supplementary Figure S2G). PCR primers:
839 GTGGTGCCTGAGGTGGTGCC/CCACTCCCAAAATGGGGCCG
840 Successful labeling of SRRM2 only was confirmed by the reduction of mVenus by two
841 individual shRNAs directed against SRRM2 (Supplementary Figure S5A).

842 **ArgRS, MetRS, and SRRM2 knock down**

843 shRNAs against ArgRS (shRARS_1: gtggacacaagcataagtaaa, shRARS_2:
844 ggagcagttacaagaagaaaa) were cloned into a pLKO.1 vector (pLKO.1 - TRC cloning vector

845 was a gift from David Root, Addgene plasmid #10878; http://n2t.net/addgene:10878;
846 RRID:Addgene_10878 (Moffat et al., 2006)). A non-targeting control shRNA pLKO.1 shSCR
847 was a gift from Sheila Stewart (Addgene plasmid #17920; http://n2t.net/addgene:17920;
848 RRID:Addgene_17920 (Saharia et al., 2008)). shRNAs against *SRRM2* and *MARS* were
849 acquired from The RNAi Consortium *via* Sigma Aldrich (shSRRM2_1:
850 cgccacctaaacagaaatc, shSRRM2_2: gttgggactggaggttgta, shMARS_1:
851 caaggaaacattgtccgagaac, shMARS_2: tcgacatggcaaccaatatatc). Plasmids were co-
852 transfected into 293T cells together with lentiviral packaging plasmids pRSV-rev,
853 pMDLg/pRRE, and pMD2.G (plasmids were a gift from Didier Trono (Addgene plasmid
854 #12253 and #12251; http://n2t.net/addgene:12253 and :12251; RRID:Addgene_12253 and
855 _12251 (Dull et al., 1998)), and a gift from the Torbett lab at Scripps Research) using
856 Lipofectamine 2000 (Invitrogen). Medium was changed after overnight transfection and
857 collected two days later. Supernatant containing viral particles was filtered through a 0.45
858 µm syringe filter, and either used directly or stored at -80°C. For viral transduction, SRRM2-
859 mVenus-tagged 293T or HepG2 cells were seeded a day prior on 6 cm tissue culture dishes
860 and incubated with 1 ml undiluted viral particles in the presence of 8 µg polybrene (EMD
861 Millipore) for two hours. Afterwards, fresh medium was added, and the infection left to
862 proceed for two days. Successfully transduced cells were selected with 10 µg/ml (293T) or
863 50 µg/ml (HepG2) puromycin (AdipoGen Life Science). ArgRS knock down was confirmed
864 via western blot and quantitative real-time PCR.

865 **Reverse transcription and quantitative real-time PCR (RT-qPCR)**

866 RNA was isolated using Trizol (Invitrogen) according to the manufacturer's instructions. 500
867 ng RNA was reverse-transcribed using MultiScribe Reverse Transcriptase (Applied

868 Biosystems) according to instructions in the High-Capacity cDNA Reverse Transcription Kit
869 (Applied Biosystems) with random hexamers (Qiagen) as primers. qRT-PCR was performed
870 with Power SYBR Green Master Mix (Thermo Fisher Scientific) on a StepOnePlus (Applied
871 Biosystems). The following primers were used:
872 *RARS*: GAGAGTATAAGCCGCCTCTTTG/TCCTCCTCAGTATCAAACCTCT;
873 *SRRM2*: TGACAGCAAATCTCGACTATCC/GGTTCAGGAGAGGAATCAGAAC
874 18S: CTGAGAAACGGCTACCACATC/GCCTCGAAAGAGTCCTGTATTG
875 **Immunofluorescence**
876 Glass coverslips (12 mm, 1.5 thickness, Neuvitro Corporation) were sterilized with 70%
877 ethanol, coated with 0.01% Collagen I (MP Biomedicals Inc) overnight, and stored in PBS
878 until use. Two days prior to staining, 10,000 HepG2 or 293T cells were seeded on coverslips.
879 Cells were washed, fixed with 4% PFA in PBS for 20 minutes, permeabilized in 0.25% Triton
880 X-100 for 5 minutes, blocked with 1% FCS, 2% BSA in PBS (IF buffer) for a minimum of 15
881 minutes, and stained overnight with anti-SRRM2 antibody or anti-ArgRS antibody (both
882 SCBT, 1:100, all dilutions in IF buffer) at 4°C. Cells were washed twice with PBS and once
883 with IF buffer between all steps. Anti-mouse AlexaFluor 488 secondary antibody (Abcam)
884 was diluted 1:250 and added to the cells for 45 minutes at room temperature. Anti-
885 SC35/SFRS2 (Proteintech), Methionine-tRNA Synthetase (MetRS, Abcam), or Arginyl-tRNA
886 Synthetase antibody (Biorbyt) were added at a 1:100 dilution (ArgRS) or 1:200 dilution
887 (MetRS, SC35) and incubated at room temperature for 3 hours. Cross-adsorbed anti-rabbit
888 Alexa Fluor 568 secondary antibody (Abcam) was added for 45 minutes at room temperature
889 at a dilution of 1:250. Hoechst 33342 (AdipoGen Life Science) was added at 1:500 in PBS
890 for 15 minutes. Cover slips were washed in PBS, dipped in water, mounted on soft-set

891 Vectashield (Vectorlabs), and sealed with gel glue or nailpolish. Slides were stored at 4°C
892 until imaging.

893 **Confocal microscopy and colocalization**

894 Microscopes were maintained by the Core Microscopy Facility at Scripps Research. For co-
895 localization of SRRM2, ArgRS, SFPQ, and MetRS, a Zeiss LSM 880 Airyscan confocal laser
896 scanning microscope with a 100x oil objective was used for imaging in airyscan mode.
897 Confocal images were recorded with a pixel dwell time of 1.5 µs in 16-bit depth with a scaling
898 of 0.034 µm (x, y) and 0.145 µm (z). Z-stacks covering the nucleus were taken with a
899 motorized stage. Images were processed with "Airyscan Processing" in Zen (Zeiss).
900 Estimation of colocalization was done with Imaris (Oxford Instruments). First, the nuclear
901 volume of each cell was determined by using Hoechst DNA staining as a mask to delineate
902 the cell nucleus, with an adequate threshold to filter spillover of Hoechst signal. Second, the
903 nuclear signal of two antibody stains were colocalized by comparing nuclear volumes in
904 individual cells and the percentage of colocalized volume was noted as well as Manders
905 overlap coefficients and Pearson correlation coefficient. Manders overlap coefficient
906 calculates the overlap between two colors from their absolute intensities and results in
907 individual coefficients for each color (co-occurrence of color1 with color2 and vice versa). In
908 contrast, Pearson correlation coefficient uses the deviation from the mean and results
909 therefore in one coefficient for the correlation between both colors (relationship between the
910 signal intensities). Background for the antibody staining was determined by comparison of
911 signal intensity to a control in which cells were stained with secondary antibody only or by
912 Costes thresholding in Imaris, if stated so in the figure legend. Videos demonstrating
913 colocalization (Supplementary Videos 1-4) were recorded with Imaris (Oxford Instruments).

914 Supplementary Figure S2H was taken on a Zeiss LSM 710 confocal laser scanning
915 microscope with a 63x oil objective.

916 **Fluorescence recovery after photobleaching (FRAP)**

917 SRRM2-mVenus 293T cells expressing either a non-targeting control shRNA (shSCR ctrl)
918 or shRNA against ArgRS (shRARS) were seeded on collagen-I coated (as described above
919 for cover slips) glass bottom 35 mm dishes with 1.5 thickness (World Precision Instrument)
920 two days prior to imaging. Live cell imaging was performed on a Zeiss LSM 780 or a LSM
921 880 confocal laser scanning microscope at 37°C, 5% CO_2 with a 63x water objective.
922 Fluorescent bleaching was achieved by 20 cycles of 100% intensity at 514 nm. Pictures
923 were taken every 2 s for 75 cycles with a pixel dwell time of 1.58 µs and fluorescence in
924 regions of interest (ROIs) were recorded with ZEN (Zeiss). The resulting data was subtracted
925 from background, divided by fluorescence intensity of the same area before bleaching
926 (normalization), and the geometric mean of ROIs was fitted with a one-exponential model to
927 calculate the half-time of fluorescence recovery (GraphPad Prism 5). The mean of individual
928 measurements was calculated and plotted together with standard error means. Pictures
929 were exported with Fiji/ImageJ. Immobile fractions were calculated from dedicated
930 measurements with images taken every 10 s (as opposed to every 2 s for the calculation of
931 half-time of recovery) to minimalize photobleaching during imaging (at the cost of temporal
932 resolution). FRAP recordings were excluded if sample drift was noted during the recording.
933 Significance was tested with a two-tailed Student's t-test (GraphPad Prism 5). We compared
934 SRRM2-mVenus fluorescence recovery half-times to known literature values of ASF/SRSF1
935 (Phair and Misteli, 2000) recovery. Secondary structure prediction of both proteins was
936 carried out with Sable (Adamczak et al., 2004).

937 **Flow cytometry and fluorescence activated cell sorting**

938 Flow cytometry was performed on instruments maintained by the Flow Cytometry core at
939 Scripps Research. 293T cells were detached using Trypsin/EDTA and resuspended in
940 DMEM with 10% FBS. The cell suspension was mixed 1:1 with sorting buffer (2.5 mM EDTA,
941 25 mM HEPES, pH 7.0, 1% FBS, 1% penicillin/streptomycin in PBS) and analyzed on an
942 LSR II analytical flow cytometer (BD Bioscience). mVenus fluorescence was detected in the
943 FITC channel (filter 525/50) after excitation by a 488 nm laser. Flow cytometry results were
944 analyzed with FlowJo version 10.06 or higher. Fluorescence activated cell sorting was
945 performed by members of the Scripps Research Flow Cytometry core on a MoFlo Astrios
946 EQ jet-in-air sorting flow cytometer (Beckman Coulter). Two days after transfection, cells
947 were detached using Accutase (Stemcell Technologies), resuspended in DMEM with FBS,
948 and spun down to remove serum to prevent cells from adhering. Following a wash with PBS,
949 cells were diluted in sorting buffer to $1x10^6$ cells/ml. Single cells were sorted into a 96 well
950 plate prefilled with 100 µL medium and expanded to monoclonal cell lines. For quantification
951 of MHCI expression, cells were detached with EDTA and stained with 1 ug/ml HB-95 W6/32
952 for 20 minutes on ice followed by Alexa 647-cojugated anti-mouse secondary antibody for
953 20 minutes on ice, both in sorting buffer.

954 **Cell viability**

955 Cell viability and proliferation was assessed by measuring AlamarBlue (AbD Serotec)
956 conversion. HepG2 or 293T cells were seeded in 96-well plates (10,000 cells/well) and 1:100
957 AlamarBlue was added two hours prior to measurement on a Synergy H1 (Biotek, λ_{exc} 530
958 nm, λ_{em} 580 nm). All measurements were done in technical quadruplicates.

959 **RNA isolation and TGIRT-seq library preparation**

960 $2.5x10^6$ HepG2 cells expressing either a non-targeting shRNA control (shSCR) or a shRNA
961 directed against ArgRS (gene name: *RARS*, shRARS) were seeded on 10 cm tissue culture
962 dishes two days prior to RNA isolation. Cells were starved off arginine for 6 hours and
963 supplemented with 10x arginine two hours prior to harvest. RNA was isolated by using a
964 mirVana miRNA isolation kit (Invitrogen) with phenol extraction following the manufacturer's
965 instruction for total RNA isolation. RNA integrity was evaluated with a Bioanalyzer (Agilent).
966 Extracted total RNA was treated with TURBO DNase (Thermo Fisher) according to the
967 manufacturer's instruction, and the DNase-treated RNA was then ribo-depleted by using a
968 Ribo-Zero Gold (Human/Mouse/Rat) kit (Illumina). For each library, 50 ng of ribo-depleted
969 RNA was fragmented by using an RNA Fragmentation Module kit (New England Biolabs) to
970 a median size of 55-75 nt, and 3' phosphates were removed by treatment with T4
971 polynucleotide kinase (Epicentre).
972 TGIRT-seq libraries were prepared essentially as described (Qin et al., 2016) using a
973 modified R2R adapter that decreases adapter dimer formation (Xu et al., 2019). Reverse
974 transcription reactions contained fragmented, dephosphorylated cellular RNA, 100 nM R2
975 RNA/R2R DNA starter duplex, and 1 μM TGIRT-III (InGex) in reaction buffer (20 mM Tris-
976 HCl, pH 7.5, 450 mM NaCl, 5 mM $MgCl_2$, 5 mM DTT). Reactions were pre-incubated at room
977 temperature for 30 min and then initiated by addition of 1 mM dNTPs (an equimolar mix of
978 1 mM dATP, dCTP, dGTP, and dTTP) and raising the temperature to 60°C. Reverse
979 transcription by TGIRT-III is initiated by template switching from a starting duplex consisting
980 of a 35 nt DNA primer encoding the reverse complement of the Illumina Read 2 sequencing
981 primer binding site (R2R) annealed to a 34-nt complementary RNA oligonucleotide (R2),
982 leaving a single nucleotide 3' DNA overhang composed of an equimolar mixture of A, G, C

983 and T. The RNA oligonucleotide is blocked at its 3' end with C3Sp (IDT) to inhibit template
984 switching to itself. Reactions were incubated at 60°C for 15 min and terminated by adding 5
985 N NaOH to a final concentration of 0.25 N and incubating at 95°C for 3 min to degrade RNAs
986 and denature protein. The reactions were then cooled to room temperature and neutralized
987 with 5 N HCl. cDNAs were purified by using a Qiagen MinElute Reaction Cleanup Kit and
988 then ligated at their 3' ends to a DNA oligonucleotide encoding the reverse complement of
989 the Illumina Read 1 primer binding site (R1R) using Thermostable 5' AppDNA/RNA Ligase
990 (New England Biolabs). Ligated cDNAs were re-purified with a MinElute Reaction Cleanup
991 Kit and amplified by PCR for 12 cycles using Phusion DNA polymerase (Thermo Fisher
992 Scientific) with overlapping multiplex and index primers that add sequences necessary for
993 Illumina sequencing. PCR products were purified with AMPure XP beads (Beckman-Coulter)
994 to remove unused PCR primers and adaptor dimers. Libraries were sequenced on a
995 NextSeq 500 instrument (2x75 nt, paired end reads) at the Genomic Sequencing and
996 Analysis Facility at the University of Texas at Austin.

997 **TGIRT-seq bioinformatic analysis**

998 After sequencing, Fastq files were processed by using the TGIRT-map pipeline (Wu et al.,
999 2018). Briefly, the sequencing adapters were removed with Atropos (Didion et al., 2017)
1000 using options *trim -U 1 --minimum-length=15 --threads=24 --no-cache-adapters --error-*
1001 *rate=0.1 –b AAGATCGGAAGAGCACACGTCTGAACTCCAGTCAC -B*
1002 *GATCGTCGGACTGTAGAACTCTGAACGTGTAGA.* Trimmed reads were then aligned
1003 against 5S rRNA (GenBank accession: X12811.1), complete rRNA repeat unit (GenBank
1004 accession U13369.1) and hg19 Genomic tRNA database (Chan and Lowe, 2016) using
1005 BOWTIE2 (Langmead and Salzberg, 2012). The remaining unaligned reads were then

1006 sequentially aligned to the human genome (hg19) using a splice-aware aligner (HISAT2)
1007 (Kim et al., 2015) and a sensitive local aligner (BOWTIE2) (Langmead and Salzberg, 2012).
1008 Finally, gene quantification was done on genomic loci, except for tRNA and rRNA, which
1009 required an additional step of re-aligning and counting (Supplementary Table S14).
1010 Differential gene expression analysis was done using DESeq2 (Love et al., 2014). Exon
1011 quantification was done by FeatureCount (Liao et al., 2014) and differential exon usage was
1012 quantified using DEXSeq (Anders et al., 2012). DEXSeq uses a negative binomial model to
1013 test for differential exon usage between two samples while normalizing for the differences
1014 in gene expression (Anders et al., 2012). Gene names were assigned using biomaRt
1015 (Durinck et al., 2009).

1016 **Poly(A) RNA-seq library preparation and bioinformatic analysis**

1017 Poly(A) RNA-seq libraries were prepared and sequenced by the Genomic Sequencing and
1018 Analysis Facility at the University of Texas at Austin. RNAs were selected by using a Poly(A)
1019 Purist MAG Kit (Thermo Fisher, AM1922) using the manufacturer's protocol followed by
1020 library preparation using a NEBNext Ultra II Directional RNA Library Kit for Illumina (New
1021 England Biolabs, E7760), also following the manufacturer's protocol. Samples were
1022 sequenced on a NovaSeq 6000 instrument using SP flowcells (2x150 nt, paired end reads).
1023 Reads were trimmed with trimgalore and aligned to grch37 with STAR (Dobin et al., 2013)
1024 (Supplementary Table S15). Counts were generated with Subread (Liao et al., 2014).
1025 Differential exon usage analysis was performed with DEXSeq (Anders et al., 2012). If exons
1026 were assigned to overlapping genes, gene symbols were assigned to the first gene and
1027 counted as one gene except in the direct comparison between DEXSeq results and N-
1028 terminal peptides, were all genes were used. Differentially expressed genes were identified

1029 with DESeq2 (Love et al., 2014). Enrichment analysis was performed using Panther (Mi et
1030 al., 2019) and ShinyGO (Ge et al., 2020). For Panther, all genes mapped to grch37 were
1031 used as a reference list. Vast-tools was used to identify differentially spliced events,
1032 including cassette exons, microexons, 3' and 5' alternative splice sites, and retained splice
1033 sites (Irimia et al., 2014). Untrimmed reads were first aligned to the hg19 assembly and PSI
1034 values for all annotated splicing events were measured for each sample. Events were
1035 considered if, in at least of half of the profiled samples, they had ≥ 15 reads overlapping the
1036 included/excluded splice junctions and a ratio of reads mapping to the upstream and
1037 downstream junctions (a balance score) of < 2 or 2 to 5. These events were than processed
1038 through the vast-tools diff module (Han et al., 2017), which calculates the predicted ΔPSI
1039 between samples and assigns a minimum ΔPSI value (MV), with a ≥ 0.95 probability, for
1040 each event. For example, MV > 0 |ΔPSI| ≥ 0.1 indicates ≥ 0.95 probability of at least a 10%
1041 difference in splice junction usage in either direction.

1042 **RT-PCR for verification of splicing events**

1043 RNA was reverse transcribed and amplified using OneStep RT-PCR (Qiagen) according to
1044 the manufacturer's instructions but in a reduced volume (10 µl final). 40 ng of HepG2 RNA
1045 or 100 ng of 293T RNA were transcribed per reaction. Primers were designed using VastDB
1046 (Tapial et al., 2017) for splice junction changes and manually for differential exon usage.
1047 Amplified regions of different splice isoforms were separated on a 2.5% agarose/TAE gel
1048 and visualized after staining with SybrSafe on a Biorad ChemiDoc Imager.

1049 **Detection of N-terminal peptides**

1050 A modified protocol for the Terminal amine isotopic labeling of substrate (TAILS) was used
1051 to enrich for N-terminal peptides (Kleifeld et al., 2011). Cells were lysed, proteins were

1052 extracted by a methanol/chloroform precipitation, and N-termini were blocked overnight with
1053 formaldehyde. Proteins were extracted again with methanol/chloroform to avoid carry-over
1054 of reactive formaldehyde and digested with trypsin overnight. HPG-ALD Polymers were
1055 acquired through Flintbox and added to the peptides at a 1:50 ratio to deplete peptides with
1056 unblocked reactive N-termini derived from the trypsin digest. The next day, the reaction was
1057 quenched, and free peptides separated from the polymer with a 10 kDa spin filter. Peptides
1058 were fractionated with Pierce High pH Reversed-Phase Peptide Fractionation kit (Thermo)
1059 according to the manufacturer's instructions, all 9 fractions were dried down, resuspended
1060 in 5% acetonitrile and 0.1% formic acid and were analyzed on the Q Exactive mass
1061 spectrometer as described above. Raw data was processed with MaxQuant (Cox and Mann,
1062 2008) with dimethyllysine and dimethylated N-termini as a fixed modification. Peptides were
1063 searched against a reference proteome (Uniprot) with free N-termini and ArgC as protease
1064 and label free quantification was used with default settings. The resulting intensities and
1065 LFQ values were filtered in Perseus (Tyanova et al., 2016) against a contaminant database.
1066 Reverse and peptides preceded by arginine, which are likely derived from trypsin cleavage,
1067 were excluded. MaxQuant (version 1.6.7.0) was run on the Scripps High Performance
1068 Computing core. Genes with overlapping differential exon usage (DEXSeq padj < 0.05) and
1069 N-terminal peptides (Student's t-test difference > |Δ1|) were further manually analyzed to
1070 identify the position of the differential exon in the gene and the resulting peptide sequence.

1071 **IDH and proteasome activity**

1072 10,000 HepG2 cells were seeded in white 96 well plates two days prior to both assays. For
1073 IDH activity, cells were lysed in co-immunoprecipitation lysis buffer and mixed with an end
1074 concentration of 100 μM NADP, 2 mM $MnCl_2$, and 5 mM isocitrate. IDH activity was

1075 measured by monitoring fluorescence at 460 nm after excitation at 340 nm, once per minute
1076 for 10 minutes at 37°C. Proteasomal subunit β5 activity was measured using the
1077 ProteasomeGlo assay (Promega) according to the manufacturer's instructions in the same
1078 format. Total protein concentration (IDH, with BCA assay) or cell count (β5 activity, with
1079 alamar blue assay) were used to normalize between treatment conditions.

1080 **MHCI peptidome**

1081 $5x10^8$ cells were seeded per replicate 2 days prior to harvest and frozen at -80°C until MHCI
1082 peptide enrichment. HB-95 W6/32 hybridoma were acquired by ATCC, cultured in DMEM
1083 with 10% FBS, and diluted in HyClone CDM4MAb serum free media stepwise till 10 %
1084 DMEM was reached. Cells were left to condition the serum-reduced media for 5 days. 300
1085 ml of medium were loaded on 3 ml of Protein A, washed with PBS, and eluted with 100 mM
1086 glycine, pH 3.0, into a final concentration of 130 mM Hepes, pH 7.5 in 5 column volumes.
1087 Coupling of antibody to protein A was performed as described previously (Purcell et al.,
1088 2019). Cell lysis followed instructions by Purcell et al., but centrifugation speed was changed
1089 to 40,000 x g for 30 minutes. Separation of MHCI from MHCI-bound peptides was performed
1090 as described previously (Bassani-Sternberg et al., 2015). Peptides were measured on a QE-
1091 HFX and searched against the human proteome with ProLuCID (Xu et al., 2015) without
1092 protease specificity and no requirements for tryptic peptides for protein identification. The
1093 percentage of arginine in the proteins from which the MHCI peptides originated was not
1094 significantly changed between groups. MHCI immunogenicity score was calculated as
1095 described previously (Calis et al., 2013).

1096

1097

1098 **KEY RESOURCES TABLE**

REAGENT or RESOURCE	SOURCE	IDENTIFIER
Antibodies		
ArgRS	Biorbyt	orb247357
SRRM2	SCBT	sc-390315
MetRS	Abcam	ab31541
GFP	Proteintech	10087-514
SFSR2	Proteintech	20371-1-AP
GAPDH	CST	2118L
Histone H3	CST	9715S
Tubulin	CST	2144S
Anti-Rabbit HRP	Invitrogen	31464
Anti-Mouse HRP	Invitrogen	PI31432
Anti-Rabbit Alexa 568	Abcam	ab175696-500ug
Anti-Mouse Alexa 488	Abcam	ab150113-500ug
Bacterial and Virus Strains		
DH5alpha	NEB	C2987H
Top10	Invitrogen	C404010
ClearColi	Lucigen	89428-536
Biological Samples		
Chemicals, Peptides, and Recombinant Proteins		
Marfey's Reagent	Pierce	PI48895
Murine Arginase-1	This paper	N/A
Hoechst 33342	Adipogen	50596053
Carbon tetrachloride (CCl_4)	Sigma-Aldrich	270652-100ML
13C6-arginine	Pierce	PI88210
Alamar Blue	Biorad	BUF012A
HPG-ALD Polymers	Flintbox UBC	N/A
T4 Polynuclotide Kinase, Cloned	Lucigen	P0503K
TGIRT-III	Ingex	TGIRT™-III Enzyme
Thermostable 5' App DNA/RNA Ligase	New England Biolabs	M0319
Phusion High Fidelity PCR Master Mix with HF Buffer	Thermo Scientific	F531
TGIRT III	Ingex	TGIRT™-III Enzyme
Critical Commercial Assays		
Co-IP kit	Pierce	PI26149
mirVana RNA isolation	Life Technologies	AM1560
OneStep RT PCR	Qiagen	210210
NEBNext Magnesium RNA Fragmentation Module	New England Biolabs	E6150S
5' DNA Adenylation Kit	New England Biolabs	E2610
NEBNext Ultra II Directional RNA Kit for Illumina	New England Biolabs	E7760
Poly(A)Purist MAG Kit	Invitrogen	AM1922
RNA Clean & Concentrator-5 Kit	Zymo Research	R1013
Oligo Clean & Concentrator Kit	Zymo Research	D4060
MinElute Reaction Cleanup Kit	Qiagen	28206
Pierce High pH Reversed-Phase Peptide Fractionation kit	Thermo Scientific	84868
Proteasome-Glo Assays	Promega	G8621
Deposited Data		
TGIRT-seq data	This paper	SRA PRJNA561913

Poly(A) RNA-seq	This paper	GEO GSE165513
ArgRS interactome	This paper	Pride PXD015692
MetRS interactome	Cui et al., 2020	Pride PXD021527
N-terminomics	This paper	Pride PXD024091
MHCI peptidome	This paper	Pride PXD027531
Experimental Models: Cell Lines		
HepG2	ATCC	HB-8065, verified by ATCC
HEK 293T	ATCC	CRL-3216, verified by ATCC
W6/32	ATCC	HB-95
Murine embryonic fibroblasts	Dr. Yao Tong Scripps Research	N/A
Experimental Models: Organisms/Strains		
C57Bl/6J	Scripps Breeding Colony	N/A
Oligonucleotides		
gRNA SRRM2 CCAUGAGACACCGCUCCUCC	Eton Bioscience	N/A
shRNA RARS (3'UTR) gtggacacaagcataagtaaa	Eton Bioscience	N/A
shRNA RARS (CDS) ggagcagttacaagaagaaaa	Eton Bioscience	N/A
All other oligos	Eton Bioscience	N/A
TGIRT-seq: starting molecule Read2 oligonucleotides	IDT Bioscience, Xu et al. 2019	NTT R2R DNA/R2 RNA
TGIRT-seq: 5' phosphorylated Read1 oligonucleotide	IDT Bioscience, Xu et al. 2019	R1R DNA
Recombinant DNA		
pSpCas9(BB)-2A-GFP_SRRM2	This paper	N/A
mVenus donor for SRRM2	This paper	N/A
pLKO.1 shRARS_3UTR	This paper	N/A
pLKO.1 shRARS_2	This paper	N/A
pSpCas9(BB)-2A-GFP (PX458)	Ran et al., 2013	Addgene 48138
pLKO.1 shSCR	Saharia et al., 2008	Addgene 17920
pLKO.1 shSRRM2_1, _2	Sigma Aldrich	TRCN0000314562, TRCN0000314504
pLKO.1 shMARS_1, _2	Sigma Aldrich	TRCN0000298212, TRCN0000293830
Software and Algorithms		
Imaris	Bitplane	https://imaris.oxinst.com/
Fiji	Schindelin et al., 2012	https://imagej.net/Fiji
Hisat2	Kim et al., 2015	http://daehwankimlab.github.io/hisat2/
Bowtie2	Langmead and Salzberg, 2012	http://bowtie-bio.sourceforge.net/bowtie2/index.shtml
Trimgalore	Felix Krueger	https://www.bioinformatics.babraham.ac.uk/projects/trim_galore/

Subread	Liao et al., 2014	https://bioconductor.org/packages/release/bioc/html/Rsubread.html
DESeq2	Love et al., 2014	http://bioconductor.org/packages/release/bioc/html/DESeq2.html
DEXseq	Anders et al., 2012	https://bioconductor.org/packages/release/bioc/html/DEXSeq.html
Vast-Tools	Irimia et al., 2014	https://github.com/vastgroup/vast-tools
Vast Tools Diff module	Han et al., 2017	https://github.com/vastgroup/vast-tools
VastDB	Tapial et al., 2017	http://vastdb.crg.eu/wiki/Main_Page
Panther	Mi et al., 2019	http://pantherdb.org/
ShinyGO	Ge et al., 2020	http://bioinformatics.sdstate.edu/go/
Maxquant	Cox,J. and Mann,M., 2008	https://www.maxquant.org/
Perseus	Tyanova et al., 2016	https://maxquant.net/perseus/
GraphPad Prism 7-9	GraphPad Software LLC	https://www.graphpad.com/
R Studio	R Studio	https://rstudio.com/
Tidyverse	Tidyverse/RStudio	https://www.tidyverse.org/
biomaRt	Durinck S et al., 2009	https://bioconductor.org/packages/release/bioc/html/biomaRt.html
EnhancedVolcano	Blighe K, Rana S, Lewis M, 2020	https://bioconductor.org/packages/release/bioc/html/EnhancedVolcano.html
TGIRTseq pipeline	Douglas C. Wu	https://github.com/wckdouglas/tgirt_map
ggpubr	Alboukadel Kassambara	https://CRAN.R-project.org/package=ggpubr
Subread to DEXSeq	Vivek Bhardwaj	https://github.com/vivekbhr/Subread_to_DEXSeq
ProLuCID	Xu et al., 2015	http://ip2.scripps.edu
Class I Immunogenicity	Calis et al., 2013	http://tools.iedb.org/immunogenicity/
Other		

Supplementary Information

1101 **Supplementary Figures 1-7**

1102 **Supplementary tables**

1103 Table S1: ArgRS nuclear interactome in HepG2.

1104 Table S2: ArgRS interactome in HepG2 whole cell lysate.

1105 Table S3: ArgRS interactome in 293T whole cell lysate.

1106 Table S4: MetRS interactome in 293T whole cell lysate.

1107 Table S5: Proteins shared between interactomes.

1108 Table S6: tRNA expression upon ArgRS knock down as calculated from TGIRTseq.

1109 Table S7: Splice junctions with MV > 0 and |ΔPSI| > 0.1 upon ArgRS knock down.

1110 Table S8: Differentially expressed exons upon ArgRS knock down (padj > 0.05).

1111 Table S9: Peptides identified after enrichment of N-terminal peptides with |pDiff| > 1 upon

1112 ArgRS knock down.

1113 Table S10: Splice junctions with MV > 0 and |ΔPSI| > 0.1 upon SRRM2 knock down.

1114 Table S11: Differentially expressed exons upon SRRM2 knock down (padj > 0.05).

1115 Table S12: Splice junctions with MV > 0 and |ΔPSI| > 0.1 upon MetRS knock down.

1116 Table S13: Genes associated with Hallmark and GO terms that are inversely modulated by

1117 ArgRS and SRRM2.

1118 Table S14: Mapping statistics for TGIRT-seq. Numbers on the top of each cell represent

1119 numbers of read pairs. Numbers within parentheses represent percentages. Raw pairs

1120 indicate the number of read pairs for the sample after Illumina sample demultiplexing.

1121 Trimmed pairs indicate the number of read pairs that passed adapter- and quality- trimmings,

1122 and length-cutoffs, number in parentheses indicates percentage of trimmed pairs respect to

1123 raw pairs. tRNA/rRNA pairs indicates number of read pairs that can be concordantly aligned

1124 to ribosomal RNA repeat units (GenBank accession numbers: X12811.1 and U13369.1)) or
1125 tRNA (GtRNAdb; (Chan and Lowe, 2016), percentage is computed respect to trimmed pairs.
1126 Non tRNA/rRNA pairs indicate the number of read pairs that are not mappable to rRNA or
1127 tRNA, percentage is computed respect to trimmed pairs. HISAT2 mapped pairs indicates
1128 number of read pairs that can be aligned concordantly to human genome (hg19) by HISAT2
1129 (Kim et al., 2015), percentage is computed respect to non tRNA/rRNA pairs. BOWTIE2
1130 mapped pairs indicates number of read pairs that aligned to human genome by BOWTIE2
1131 (Langmead and Salzberg, 2012), percentage is computed respect to non tRNA/rRNA pairs.
1132 Mapping rate is computed by the sum of percentage of HISAT mapper pairs and BOWTIE2
1133 mapped pairs. Uniquely mapped indicates number of read pairs that are aligned to the
1134 human genome at a single location without ambiguity by HISAT2 (with alignment tag NH:1)
1135 or BOWTIE2 (MAPQ = 255). Unique map rate is computed respective to the sum of HISAT
1136 mapped pairs and BOWTIE2 mapped pairs. Splice read rate is computed by dividing the
1137 number of read pairs with either read being split by HISAT2 aligner (with a N cigar string) to
1138 the sum of HISAT mapped pairs and BOWTIE2 mapped pairs.
1139 Table S15: Mapping statistics for RNA-seq.
1140
1141 **Supplementary videos**
1142 Video S1: SC35/SRRM2 distribution in the nucleus. Visualization of SC35 and SRRM2
1143 signal in a HepG2 hepatocellular carcinoma cell by immunofluorescent staining. Blue:
1144 Hoechst staining of DNA; green: SRRM2; red: SC35, yellow: colocalization. Sequence in
1145 video: SC35 only – SRRM2 only – SC35 and SRRM2 – SC35 and SRRM2, colocalized
1146 areas highlighted in yellow.

1147 Video S2: ArgRS/SRRM2 colocalization in the nucleus. Visualization of ArgRS and SRRM2
1148 nuclear signal in a HepG2 hepatocellular carcinoma cell by immunofluorescent staining. The
1149 cell nucleus was identified by Hoechst staining. Blue: Hoechst staining of DNA; red: ArgRS;
1150 green: SRRM2; yellow: colocalization between ArgRS and SRRM2. Sequence in video:
1151 ArgRS only - SRRM2 only - ArgRS and SRRM2 – ArgRS and SRRM2, colocalized areas
1152 highlighted in yellow.
1153 Video S3: MetRS/SRRM2 colocalization in the nucleus. Visualization of MetRS and SRRM2
1154 nuclear signal in a HepG2 hepatocellular carcinoma cell by immunofluorescent staining. The
1155 cell nucleus was identified by Hoechst staining. Blue: Hoechst staining of DNA; red: MetRS;
1156 green: SRRM2; yellow: colocalization between MetRS and SRRM2. Sequence in video:
1157 MetRS only - SRRM2 only - MetRS and SRRM2 – MetRS and SRRM2, colocalized areas
1158 highlighted in yellow.
1159 Video S4: MetRS/ArgRS colocalization in the cell. Visualization of ArgRS and MetRS in a
1160 HepG2 hepatocellular carcinoma cell by immunofluorescent staining. The cell nucleus was
1161 identified by Hoechst staining. Blue: Hoechst staining of DNA; red: MetRS; green: ArgRS;
1162 yellow: colocalization between ArgRS and SRRM2. Sequence in video: MetRS only - ArgRS
1163 only - ArgRS and MetRS – ArgRS and MetRS, colocalized areas highlighted in yellow.
1164 Video S5: Fluorescence recovery after photobleaching (FRAP) of SRRM2-mVenus
1165 fluorescence in 293T cells expressing a non-targeting shRNA (ctrl). Bleaching occurs
1166 between frame 4 and 5 (1 s into the video).
1167 Video S6: Fluorescence recovery after photobleaching (FRAP) of SRRM2-mVenus
1168 fluorescence in 293T cells expressing a shRNA against the 3'UTR of ArgRS (shRARS_1).
1169 Bleaching occurs between frame 4 and 5 (1 s into the video).

1170 Video S7: Fluorescence recovery after photobleaching (FRAP) of SRRM2-mVenus
1171 fluorescence in 293T cells expressing a shRNA against the coding region of ArgRS
1172 (shRARS_2). Bleaching occurs between frame 4 and 5 (1 s into the video).

1173

1174 **References**

1175 Aass, K.R., Kastnes, M.H., and Standal, T. (2021). Molecular interactions and functions of
1176 IL-32. J. Leukoc. Biol. *109*, 143–159.

1177 Adamczak, R., Porollo, A., and Meller, J. (2004). Accurate prediction of solvent
1178 accessibility using neural networks-based regression. Proteins *56*, 753–767.

1179 Anders, S., Reyes, A., and Huber, W. (2012). Detecting differential usage of exons from
1180 RNA-seq data. Genome Res. *22*, 2008–2017.

1181 Bar-Peled, L., and Sabatini, D.M. (2014). Regulation of mTORC1 by amino acids. Trends
1182 Cell Biol. *24*, 400–406.

1183 Bassani-Sternberg, M., Pletscher-Frankild, S., Jensen, L.J., and Mann, M. (2015). Mass
1184 spectrometry of human leukocyte antigen class I peptidomes reveals strong effects of
1185 protein abundance and turnover on antigen presentation. Mol. Cell. Proteomics MCP *14*,
1186 658–673.

1187 Bertram, K., El Ayoubi, L., Dybkov, O., Agafonov, D.E., Will, C.L., Hartmuth, K., Urlaub, H.,
1188 Kastner, B., Stark, H., and Lührmann, R. (2020). Structural Insights into the Roles of
1189 Metazoan-Specific Splicing Factors in the Human Step 1 Spliceosome. Mol. Cell *80*, 127-
1190 139.e6.

1191 Blencowe, B.J. (2017). The Relationship between Alternative Splicing and Proteomic
1192 Complexity. Trends Biochem. Sci. *42*, 407–408.

1193 Blencowe, B.J., Issner, R., Nickerson, J.A., and Sharp, P.A. (1998). A coactivator of pre-
1194 mRNA splicing. Genes Dev. *12*, 996–1009.

1195 Blencowe, B.J., Baurén, G., Eldridge, A.G., Issner, R., Nickerson, J.A., Rosonina, E., and
1196 Sharp, P.A. (2000). The SRm160/300 splicing coactivator subunits. RNA N. Y. N *6*, 111–
1197 120.

1198 Boivin, V., Deschamps-Francoeur, G., Couture, S., Nottingham, R.M., Bouchard-Bourelle,
1199 P., Lambowitz, A.M., Scott, M.S., and Abou-Elela, S. (2018). Simultaneous sequencing of
1200 coding and noncoding RNA reveals a human transcriptome dominated by a small number
1201 of highly expressed noncoding genes. RNA N. Y. N *24*, 950–965.

1202 Braunschweig, U., Barbosa-Morais, N.L., Pan, Q., Nachman, E.N., Alipanahi, B.,
1203 Gonatopoulos-Pournatzis, T., Frey, B., Irimia, M., and Blencowe, B.J. (2014). Widespread
1204 intron retention in mammals functionally tunes transcriptomes. Genome Res. *24*, 1774–
1205 1786.

1206 Bronte, V., and Zanovello, P. (2005). Regulation of immune responses by L-arginine
1207 metabolism. Nat. Rev. Immunol. *5*, 641–654.

1208 Calis, J.J.A., Maybeno, M., Greenbaum, J.A., Weiskopf, D., De Silva, A.D., Sette, A.,
1209 Keşmir, C., and Peters, B. (2013). Properties of MHC class I presented peptides that
1210 enhance immunogenicity. PLoS Comput. Biol. *9*, e1003266.

1211 Chan, P.P., and Lowe, T.M. (2016). GtRNAdb 2.0: an expanded database of transfer RNA
1212 genes identified in complete and draft genomes. Nucleic Acids Res. *44*, D184-189.

1213 Chen, Y., and Belmont, A.S. (2019). Genome organization around nuclear speckles. Curr.
1214 Opin. Genet. Dev. *55*, 91–99.

1215 Costes, S.V., Daelemans, D., Cho, E.H., Dobbin, Z., Pavlakis, G., and Lockett, S. (2004).
1216 Automatic and quantitative measurement of protein-protein colocalization in live cells.
1217 Biophys. J. *86*, 3993–4003.

1218 Cox, J., and Mann, M. (2008). MaxQuant enables high peptide identification rates,
1219 individualized p.p.b.-range mass accuracies and proteome-wide protein quantification. Nat.
1220 Biotechnol. *26*, 1367–1372.

1221 Cui, H., Kapur, M., Diedrich, J.K., Yates, J.R., Ackerman, S.L., and Schimmel, P. (2021).
1222 Regulation of ex-translational activities is the primary function of the multi-tRNA synthetase
1223 complex. Nucleic Acids Res. *49*, 3603–3616.

1224 Didion, J.P., Martin, M., and Collins, F.S. (2017). Atropos: specific, sensitive, and speedy
1225 trimming of sequencing reads. PeerJ *5*, e3720.

1226 Dobin, A., Davis, C.A., Schlesinger, F., Drenkow, J., Zaleski, C., Jha, S., Batut, P.,
1227 Chaisson, M., and Gingeras, T.R. (2013). STAR: ultrafast universal RNA-seq aligner.
1228 Bioinforma. Oxf. Engl. *29*, 15–21.

1229 Dong, J., Qiu, H., Garcia-Barrio, M., Anderson, J., and Hinnebusch, A.G. (2000).
1230 Uncharged tRNA activates GCN2 by displacing the protein kinase moiety from a bipartite
1231 tRNA-binding domain. Mol. Cell *6*, 269–279.

1232 Duchon, A.A., St Gelais, C., Titkemeier, N., Hatterschide, J., Wu, L., and Musier-Forsyth,
1233 K. (2017). HIV-1 Exploits a Dynamic Multi-aminoacyl-tRNA Synthetase Complex To
1234 Enhance Viral Replication. J. Virol. *91*.

1235 Dull, T., Zufferey, R., Kelly, M., Mandel, R.J., Nguyen, M., Trono, D., and Naldini, L.
1236 (1998). A third-generation lentivirus vector with a conditional packaging system. J. Virol.
1237 *72*, 8463–8471.

1238 Durinck, S., Spellman, P.T., Birney, E., and Huber, W. (2009). Mapping identifiers for the
1239 integration of genomic datasets with the R/Bioconductor package biomaRt. Nat. Protoc. *4*,
1240 1184–1191.

1241 Galarza-Muñoz, G., Briggs, F.B.S., Evsyukova, I., Schott-Lerner, G., Kennedy, E.M.,
1242 Nyanhete, T., Wang, L., Bergamaschi, L., Widen, S.G., Tomaras, G.D., et al. (2017).
1243 Human Epistatic Interaction Controls IL7R Splicing and Increases Multiple Sclerosis Risk.
1244 Cell *169*, 72-84.e13.

1245 Galganski, L., Urbanek, M.O., and Krzyzosiak, W.J. (2017). Nuclear speckles: molecular
1246 organization, biological function and role in disease. Nucleic Acids Res. *45*, 10350–10368.

1247 Gautam, A., Grainger, R.J., Vilardell, J., Barrass, J.D., and Beggs, J.D. (2015). Cwc21p
1248 promotes the second step conformation of the spliceosome and modulates 3' splice site
1249 selection. Nucleic Acids Res. *43*, 3309–3317.

1250 Ge, S.X., Jung, D., and Yao, R. (2020). ShinyGO: a graphical gene-set enrichment tool for
1251 animals and plants. Bioinforma. Oxf. Engl. *36*, 2628–2629.

1252 Geiger, R., Rieckmann, J.C., Wolf, T., Basso, C., Feng, Y., Fuhrer, T., Kogadeeva, M.,
1253 Picotti, P., Meissner, F., Mann, M., et al. (2016). L-Arginine Modulates T Cell Metabolism
1254 and Enhances Survival and Anti-tumor Activity. Cell *167*, 829-842.e13.

1255 Guo, M., and Schimmel, P. (2013). Essential nontranslational functions of tRNA
1256 synthetases. Nat. Chem. Biol. *9*, 145–153.

1257 Guo, Y.E., Manteiga, J.C., Henninger, J.E., Sabari, B.R., Dall'Agnese, A., Hannett, N.M.,
1258 Spille, J.-H., Afeyan, L.K., Zamudio, A.V., Shrinivas, K., et al. (2019). Pol II
1259 phosphorylation regulates a switch between transcriptional and splicing condensates.
1260 Nature *572*, 543–548.

1261 Han, H., Braunschweig, U., Gonatopoulos-Pournatzis, T., Weatheritt, R.J., Hirsch, C.L.,
1262 Ha, K.C.H., Radovani, E., Nabeel-Shah, S., Sterne-Weiler, T., Wang, J., et al. (2017).
1263 Multilayered Control of Alternative Splicing Regulatory Networks by Transcription Factors.
1264 Mol. Cell *65*, 539-553.e7.

1265 Hayano, M., Yang, W.S., Corn, C.K., Pagano, N.C., and Stockwell, B.R. (2016). Loss of
1266 cysteinyl-tRNA synthetase (CARS) induces the transsulfuration pathway and inhibits
1267 ferroptosis induced by cystine deprivation. Cell Death Differ. *23*, 270–278.

1268 Hnisz, D., Shrinivas, K., Young, R.A., Chakraborty, A.K., and Sharp, P.A. (2017). A Phase
1269 Separation Model for Transcriptional Control. Cell *169*, 13–23.

1270 Horiguchi, N., Lafdil, F., Miller, A.M., Park, O., Wang, H., Rajesh, M., Mukhopadhyay, P.,
1271 Fu, X.Y., Pacher, P., and Gao, B. (2010). Dissociation between liver inflammation and
1272 hepatocellular damage induced by carbon tetrachloride in myeloid cell-specific signal
1273 transducer and activator of transcription 3 gene knockout mice. Hepatol. Baltim. Md *51*,
1274 1724–1734.

1275 Hu, S., Lv, P., Yan, Z., and Wen, B. (2019). Disruption of nuclear speckles reduces
1276 chromatin interactions in active compartments. Epigenetics Chromatin *12*, 43.

1277 Ilik, İ.A., Malszycki, M., Lübke, A.K., Schade, C., Meierhofer, D., and Aktaş, T. (2020).
1278 SON and SRRM2 are essential for nuclear speckle formation. ELife *9*, e60579.

1279 Irimia, M., Weatheritt, R.J., Ellis, J.D., Parikshak, N.N., Gonatopoulos-Pournatzis, T.,
1280 Babor, M., Quesnel-Vallières, M., Tapial, J., Raj, B., O'Hanlon, D., et al. (2014). A highly
1281 conserved program of neuronal microexons is misregulated in autistic brains. Cell *159*,
1282 1511–1523.

1283 Itsumi, M., Inoue, S., Elia, A.J., Murakami, K., Sasaki, M., Lind, E.F., Brenner, D., Harris,
1284 I.S., Chio, I.I.C., Afzal, S., et al. (2015). Idh1 protects murine hepatocytes from endotoxin-
1285 induced oxidative stress by regulating the intracellular NADP(+)/NADPH ratio. Cell Death
1286 Differ. *22*, 1837–1845.

1287 Jones, R.G., and Pearce, E.J. (2017). MenTORing Immunity: mTOR Signaling in the
1288 Development and Function of Tissue-Resident Immune Cells. Immunity *46*, 730–742.

1289 Kaminska, M., Havrylenko, S., Decottignies, P., Gillet, S., Le Maréchal, P., Negrutskii, B.,
1290 and Mirande, M. (2009). Dissection of the structural organization of the aminoacyl-tRNA
1291 synthetase complex. J. Biol. Chem. *284*, 6053–6060.

1292 Kaplanis, J., Samocha, K.E., Wiel, L., Zhang, Z., Arvai, K.J., Eberhardt, R.Y., Gallone, G.,
1293 Lelieveld, S.H., Martin, H.C., McRae, J.F., et al. (2020). Evidence for 28 genetic disorders
1294 discovered by combining healthcare and research data. Nature 1–7.

1295 Keilhauer, E.C., Hein, M.Y., and Mann, M. (2015). Accurate protein complex retrieval by
1296 affinity enrichment mass spectrometry (AE-MS) rather than affinity purification mass
1297 spectrometry (AP-MS). Mol. Cell. Proteomics MCP *14*, 120–135.

1298 Kim, M.H., and Kim, S. (2020). Chapter Six - Structures and functions of multi-tRNA
1299 synthetase complexes. In The Enzymes, L. Ribas de Pouplana, and L.S. Kaguni, eds.
1300 (Academic Press), pp. 149–173.

1301 Kim, D., Langmead, B., and Salzberg, S.L. (2015). HISAT: a fast spliced aligner with low
1302 memory requirements. Nat. Methods *12*, 357–360.

1303 Kleifeld, O., Doucet, A., Prudova, A., auf dem Keller, U., Gioia, M., Kizhakkedathu, J.N.,
1304 and Overall, C.M. (2011). Identifying and quantifying proteolytic events and the natural N
1305 terminome by terminal amine isotopic labeling of substrates. Nat. Protoc. *6*, 1578–1611.

1306 Koushik, S.V., Chen, H., Thaler, C., Puhl, H.L., and Vogel, S.S. (2006). Cerulean, Venus,
1307 and VenusY67C FRET reference standards. Biophys. J. *91*, L99–L101.

1308 Kwon, N.H., Fox, P.L., and Kim, S. (2019). Aminoacyl-tRNA synthetases as therapeutic
1309 targets. Nat. Rev. Drug Discov. *18*, 629–650.

1310 Langmead, B., and Salzberg, S.L. (2012). Fast gapped-read alignment with Bowtie 2. Nat.
1311 Methods *9*, 357–359.

1312 Lee, S.W., Cho, B.H., Park, S.G., and Kim, S. (2004). Aminoacyl-tRNA synthetase
1313 complexes: beyond translation. J. Cell Sci. *117*, 3725–3734.

1314 Liao, S.E., and Regev, O. (2021). Splicing at the phase-separated nuclear speckle
1315 interface: a model. Nucleic Acids Res. *49*, 636–645.

1316 Liao, Y., Smyth, G.K., and Shi, W. (2014). featureCounts: an efficient general purpose
1317 program for assigning sequence reads to genomic features. Bioinforma. Oxf. Engl. *30*,
1318 923–930.

1319 Love, M.I., Huber, W., and Anders, S. (2014). Moderated estimation of fold change and
1320 dispersion for RNA-seq data with DESeq2. Genome Biol. *15*, 550.

1321 Lu, S.X., De Neef, E., Thomas, J.D., Sabio, E., Rousseau, B., Gigoux, M., Knorr, D.A.,
1322 Greenbaum, B., Elhanati, Y., Hogg, S.J., et al. (2021). Pharmacologic modulation of RNA
1323 splicing enhances anti-tumor immunity. Cell *184*, 4032-4047.e31.

1324 Lund, E., and Dahlberg, J.E. (1998). Proofreading and aminoacylation of tRNAs before
1325 export from the nucleus. Science *282*, 2082–2085.

1326 Mi, H., Muruganujan, A., Ebert, D., Huang, X., and Thomas, P.D. (2019). PANTHER
1327 version 14: more genomes, a new PANTHER GO-slim and improvements in enrichment
1328 analysis tools. Nucleic Acids Res. *47*, D419–D426.

1329 Miyagawa, R., Tano, K., Mizuno, R., Nakamura, Y., Ijiri, K., Rakwal, R., Shibato, J.,
1330 Masuo, Y., Mayeda, A., Hirose, T., et al. (2012). Identification of cis- and trans-acting
1331 factors involved in the localization of MALAT-1 noncoding RNA to nuclear speckles. RNA
1332 N. Y. N *18*, 738–751.

1333 Moffat, J., Grueneberg, D.A., Yang, X., Kim, S.Y., Kloepfer, A.M., Hinkle, G., Piqani, B.,
1334 Eisenhaure, T.M., Luo, B., Grenier, J.K., et al. (2006). A lentiviral RNAi library for human
1335 and mouse genes applied to an arrayed viral high-content screen. Cell *124*, 1283–1298.

1336 Murray, P.J. (2016). Amino acid auxotrophy as a system of immunological control nodes.
1337 Nat. Immunol. *17*, 132–139.

1338 Nathanson, L., and Deutscher, M.P. (2000). Active aminoacyl-tRNA synthetases are
1339 present in nuclei as a high molecular weight multienzyme complex. J. Biol. Chem. *275*,
1340 31559–31562.

1341 Netea, M.G., Balkwill, F., Chonchol, M., Cominelli, F., Donath, M.Y., Giamarellos-
1342 Bourboulis, E.J., Golenbock, D., Gresnigt, M.S., Heneka, M.T., Hoffman, H.M., et al.
1343 (2017). A guiding map for inflammation. Nat. Immunol. *18*, 826–831.

1344 Netzer, N., Goodenbour, J.M., David, A., Dittmar, K.A., Jones, R.B., Schneider, J.R.,
1345 Boone, D., Eves, E.M., Rosner, M.R., Gibbs, J.S., et al. (2009). Innate immune and
1346 chemically triggered oxidative stress modifies translational fidelity. Nature *462*, 522–526.

1347 Nottingham, R.M., Wu, D.C., Qin, Y., Yao, J., Hunicke-Smith, S., and Lambowitz, A.M.
1348 (2016). RNA-seq of human reference RNA samples using a thermostable group II intron
1349 reverse transcriptase. RNA N. Y. N *22*, 597–613.

1350 Ofir-Birin, Y., Fang, P., Bennett, S.P., Zhang, H.-M., Wang, J., Rachmin, I., Shapiro, R.,
1351 Song, J., Dagan, A., Pozo, J., et al. (2013). Structural switch of lysyl-tRNA synthetase
1352 between translation and transcription. Mol. Cell *49*, 30–42.

1353 Pan, Q., Shai, O., Misquitta, C., Zhang, W., Saltzman, A.L., Mohammad, N., Babak, T.,
1354 Siu, H., Hughes, T.R., Morris, Q.D., et al. (2004). Revealing global regulatory features of
1355 mammalian alternative splicing using a quantitative microarray platform. Mol. Cell *16*, 929–
1356 941.

1357 Patil, M.D., Bhaumik, J., Babykutty, S., Banerjee, U.C., and Fukumura, D. (2016). Arginine
1358 dependence of tumor cells: targeting a chink in cancer's armor. Oncogene *35*, 4957–4972.

1359 Phair, R.D., and Misteli, T. (2000). High mobility of proteins in the mammalian cell nucleus.
1360 Nature *404*, 604–609.

1361 Purcell, A.W., Ramarathinam, S.H., and Ternette, N. (2019). Mass spectrometry-based
1362 identification of MHC-bound peptides for immunopeptidomics. Nat. Protoc. *14*, 1687–1707.

1363 Qin, Y., Yao, J., Wu, D.C., Nottingham, R.M., Mohr, S., Hunicke-Smith, S., and Lambowitz,
1364 A.M. (2016). High-throughput sequencing of human plasma RNA by using thermostable
1365 group II intron reverse transcriptases. RNA N. Y. N *22*, 111–128.

1366 Ran, F.A., Hsu, P.D., Wright, J., Agarwala, V., Scott, D.A., and Zhang, F. (2013). Genome
1367 engineering using the CRISPR-Cas9 system. Nat. Protoc. *8*, 2281–2308.

1368 Ray, P.S., Arif, A., and Fox, P.L. (2007). Macromolecular complexes as depots for
1369 releasable regulatory proteins. Trends Biochem. Sci. *32*, 158–164.

1370 Rock, K.L., Reits, E., and Neefjes, J. (2016). Present Yourself! By MHC Class I and MHC
1371 Class II Molecules. Trends Immunol. *37*, 724–737.

1372 Saharia, A., Guittat, L., Crocker, S., Lim, A., Steffen, M., Kulkarni, S., and Stewart, S.A.
1373 (2008). Flap endonuclease 1 contributes to telomere stability. Curr. Biol. CB *18*, 496–500.

1374 Saitoh, N., Spahr, C.S., Patterson, S.D., Bubulya, P., Neuwald, A.F., and Spector, D.L.
1375 (2004). Proteomic analysis of interchromatin granule clusters. Mol. Biol. Cell *15*, 3876–
1376 3890.

1377 Sajish, M., and Schimmel, P. (2015). A human tRNA synthetase is a potent PARP1-
1378 activating effector target for resveratrol. Nature *519*, 370–373.

1379 Sarkar, S., Azad, A.K., and Hopper, A.K. (1999). Nuclear tRNA aminoacylation and its role
1380 in nuclear export of endogenous tRNAs in Saccharomyces cerevisiae. Proc. Natl. Acad.
1381 Sci. U. S. A. *96*, 14366–14371.

1382 Saxton, R.A., Chantranupong, L., Knockenhauer, K.E., Schwartz, T.U., and Sabatini, D.M.
1383 (2016). Mechanism of arginine sensing by CASTOR1 upstream of mTORC1. Nature *536*,
1384 229–233.

1385 Schimmel, P.R., and Söll, D. (1979). Aminoacyl-tRNA synthetases: general features and
1386 recognition of transfer RNAs. Annu. Rev. Biochem. *48*, 601–648.

1387 Seburn, K.L., Nangle, L.A., Cox, G.A., Schimmel, P., and Burgess, R.W. (2006). An active
1388 dominant mutation of glycyl-tRNA synthetase causes neuropathy in a Charcot-Marie-Tooth
1389 2D mouse model. Neuron *51*, 715–726.

1390 Shehadeh, L.A., Yu, K., Wang, L., Guevara, A., Singer, C., Vance, J., and
1391 Papapetropoulos, S. (2010). SRRM2, a potential blood biomarker revealing high
1392 alternative splicing in Parkinson's disease. PloS One *5*, e9104.

1393 Shi, Y., Xu, X., Zhang, Q., Fu, G., Mo, Z., Wang, G.S., Kishi, S., and Yang, X.-L. (2014).
1394 tRNA synthetase counteracts c-Myc to develop functional vasculature. ELife *3*, e02349.

1395 Shi, Y., Wei, N., and Yang, X.-L. (2017). Studying nuclear functions of aminoacyl tRNA
1396 synthetases. Methods San Diego Calif *113*, 105–110.

1397 Shin, Y., and Brangwynne, C.P. (2017). Liquid phase condensation in cell physiology and
1398 disease. Science *357*.

1399 Son, K., You, J.-S., Yoon, M.-S., Dai, C., Kim, J.H., Khanna, N., Banerjee, A., Martinis,
1400 S.A., Han, G., Han, J.M., et al. (2019). Nontranslational function of leucyl-tRNA synthetase
1401 regulates myogenic differentiation and skeletal muscle regeneration. J. Clin. Invest. *129*,
1402 2088–2093.

1403 Spector, D.L., and Lamond, A.I. (2011). Nuclear speckles. Cold Spring Harb. Perspect.
1404 Biol. *3*.

1405 Tapial, J., Ha, K.C.H., Sterne-Weiler, T., Gohr, A., Braunschweig, U., Hermoso-Pulido, A.,
1406 Quesnel-Vallières, M., Permanyer, J., Sodaei, R., Marquez, Y., et al. (2017). An atlas of
1407 alternative splicing profiles and functional associations reveals new regulatory programs
1408 and genes that simultaneously express multiple major isoforms. Genome Res. *27*, 1759–
1409 1768.

1410 Tomsic, J., He, H., Akagi, K., Liyanarachchi, S., Pan, Q., Bertani, B., Nagy, R., Symer,
1411 D.E., Blencowe, B.J., and de la Chapelle, A. (2015). A germline mutation in SRRM2, a
1412 splicing factor gene, is implicated in papillary thyroid carcinoma predisposition. Sci. Rep. *5*,
1413 10566.

1414 Tyanova, S., Temu, T., Sinitcyn, P., Carlson, A., Hein, M.Y., Geiger, T., Mann, M., and
1415 Cox, J. (2016). The Perseus computational platform for comprehensive analysis of
1416 (prote)omics data. Nat. Methods *13*, 731–740.

1417 UniProt Consortium (2019). UniProt: a worldwide hub of protein knowledge. Nucleic Acids
1418 Res. *47*, D506–D515.

1419 Weichhart, T., Hengstschläger, M., and Linke, M. (2015). Regulation of innate immune cell
1420 function by mTOR. Nat. Rev. Immunol. *15*, 599–614.

1421 Wu, D.C., Yao, J., Ho, K.S., Lambowitz, A.M., and Wilke, C.O. (2018). Limitations of
1422 alignment-free tools in total RNA-seq quantification. BMC Genomics *19*, 510.

1423 Wyant, G.A., Abu-Remaileh, M., Wolfson, R.L., Chen, W.W., Freinkman, E., Danai, L.V.,
1424 Vander Heiden, M.G., and Sabatini, D.M. (2017). mTORC1 Activator SLC38A9 Is
1425 Required to Efflux Essential Amino Acids from Lysosomes and Use Protein as a Nutrient.
1426 Cell *171*, 642-654.e12.

1427 Xu, H., Yao, J., Wu, D.C., and Lambowitz, A.M. (2019). Improved TGIRT-seq methods for
1428 comprehensive transcriptome profiling with decreased adapter dimer formation and bias
1429 correction. Sci. Rep. *9*, 7953.

1430 Xu, T., Park, S.K., Venable, J.D., Wohlschlegel, J.A., Diedrich, J.K., Cociorva, D., Lu, B.,
1431 Liao, L., Hewel, J., Han, X., et al. (2015). ProLuCID: An improved SEQUEST-like algorithm
1432 with enhanced sensitivity and specificity. J. Proteomics *129*, 16–24.

1433 Yannay-Cohen, N., Carmi-Levy, I., Kay, G., Yang, C.M., Han, J.M., Kemeny, D.M., Kim,
1434 S., Nechushtan, H., and Razin, E. (2009). LysRS serves as a key signaling molecule in the
1435 immune response by regulating gene expression. Mol. Cell *34*, 603–611.

1436 Zhang, X., Yan, C., Hang, J., Finci, L.I., Lei, J., and Shi, Y. (2017). An Atomic Structure of
1437 the Human Spliceosome. Cell *169*, 918-929.e14.

1438 Zhu, L., and Brangwynne, C.P. (2015). Nuclear bodies: the emerging biophysics of
1439 nucleoplasmic phases. Curr. Opin. Cell Biol. *34*, 23–30.

1440

Figure 1

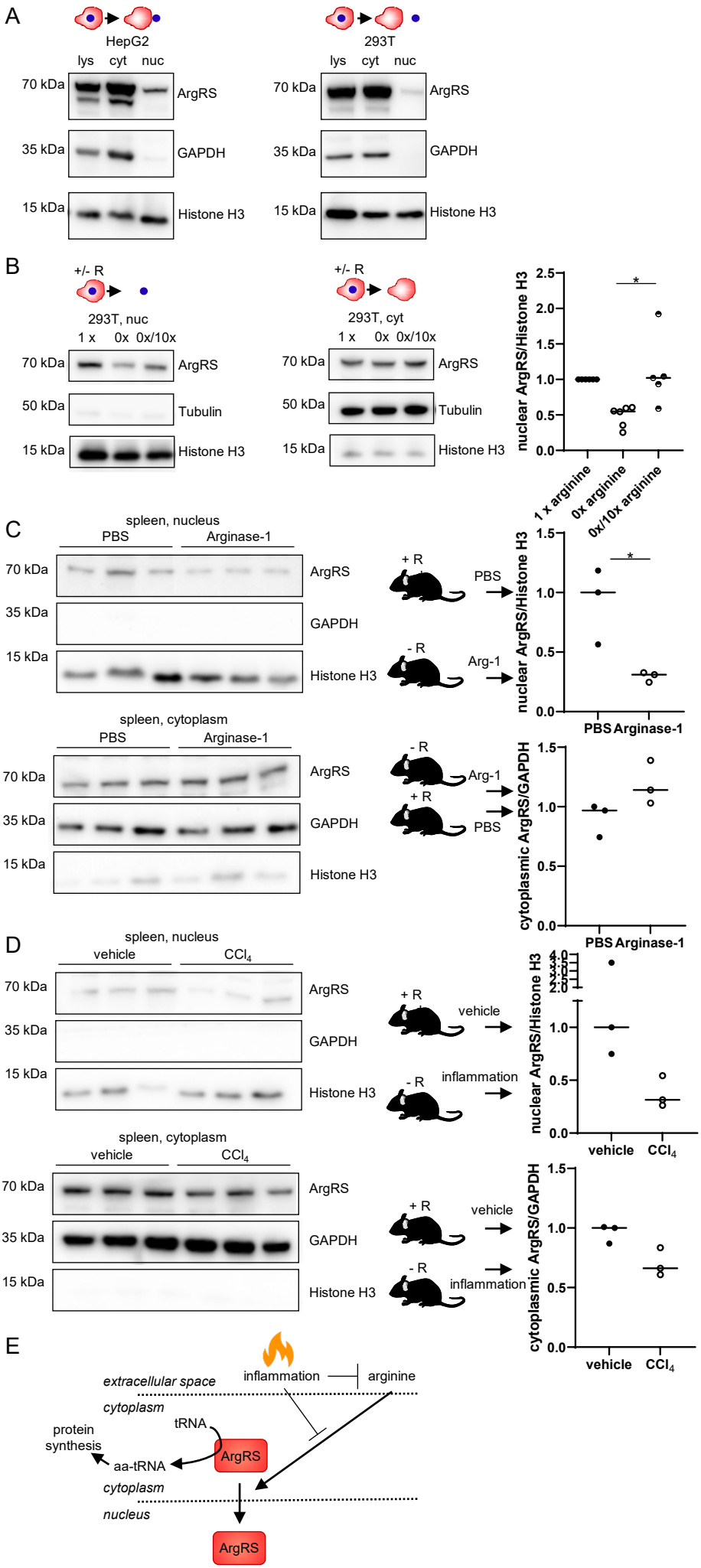
A
HepG2
lys cyt nuc
293T
lys cyt nuc
70 kDa
35 kDa
15 kDa
ArgRS
GAPDH
Histone H3
B
+/- R
293T, nuc
1 x 0x 0x/10x
293T, cyt
1 x 0x 0x/10x
50 kDa
Tubulin
nuclear ArgRS/Histone H3
1 x arginine
0x arginine
0x/10x arginine
C
spleen, nucleus
PBS
Arginase-1
+ R
- R
PBS
Arg-1
spleen, cytoplasm
cytoplasmic ArgRS/GAPDH
D
vehicle
CCl4
inflammation
E
extracellular space
inflammation
arginine
cytoplasm
tRNA
protein synthesis
aa-tRNA
ArgRS
nucleus

Figure 2

A

HepG2 nuc	HepG2 cell lysate	293T cell lysate	
ArgRS			MetRS
DECR1 (7.5)	RARS (9.1)	RARS (11.6)	EPRS (10.1)
FAM76A (7.2)	EPRS (6.7)	EPRS (8.1)	MARS (8.8)
EPRS (7.0)	FAM76A (6.2)	FAM76A (7.9)	IARS (8.8)
RARS (6.9)	AIMP1 (6.2)	AIMP1 (6.9)	AIMP1 (8.4)
DARS (6.6)	QARS (6.1)	IARS (6.9)	DARS (8.3)
AIMP1 (6.5)	SRRM2 (5.9)	SRRM2 (6.6)	RARS (8.1)
KARS (6.3)	FAM76B (5.8	DARS (6.6)	KARS (7.4)
FAM76B (5.9)	DARS (5.4)	FAM76B (6.3)	AIMP3 (6.8)
QARS (5.7)	SCYL2 (5.2)	MARS (5.8)	LARS (6.3)
IARS (5.2)	IARS (4.9)	KARS (5.7)	QARS (6.1)
AIMP2 (5.0)	LARS (4.9)	SATB2 (5.5)	AIMP2 (5.8)
SATB2 (4.9)	KARS (4.8)	SCYL2 (5.3)	
MARS (3.3)	GFPT1 (4.6)	GFPT1 (5.2)	
RPL11 (2.9)	HNRNPL (4.2)	AIMP3 (5.0)	
SRRM2 (2.3)	ERH (4.0)	CCAR2 (4.7)	
	DCTPP1 (3.6)	AIMP2 (4.2)	
	AIMP3 (3.4)	QARS (4.1)	
	PES1 (3.1)	LARS (3.2)	
	SATB2 (2.5)	MAGED1 (2.9)	
	ADD1 (2.4)	ATAD3A (2.9)	
	LRCH3 (2.1)		
	TUFM (1.7)		
	STRN3 (1.4)		
	SLC25A3 (1.0)		

B

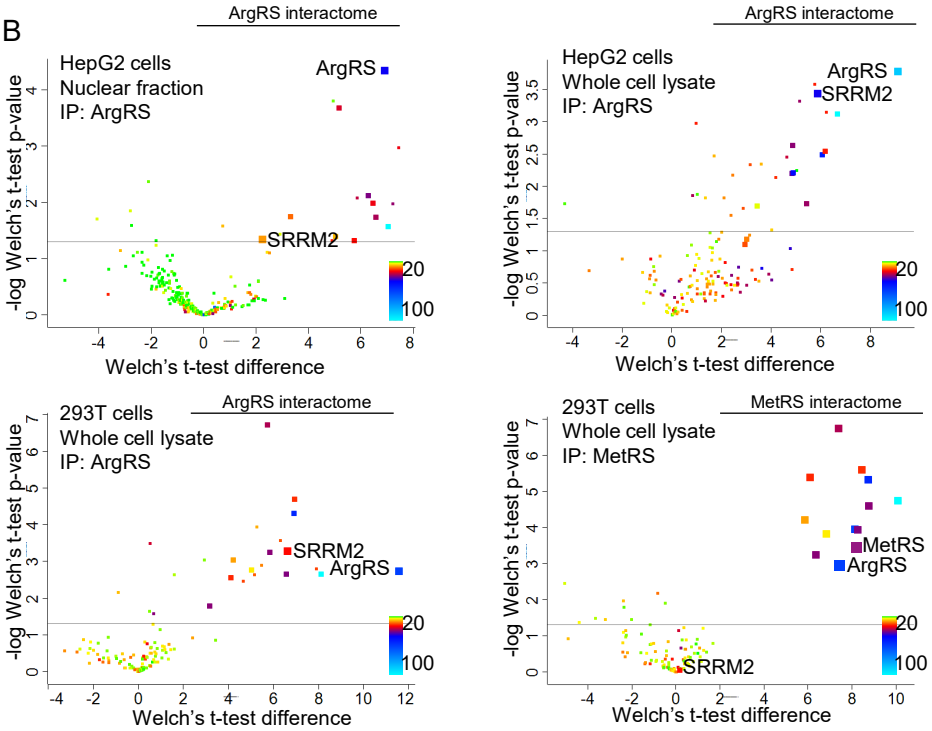

C

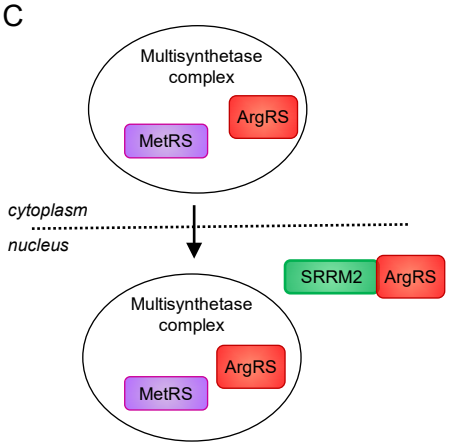

Figure 3

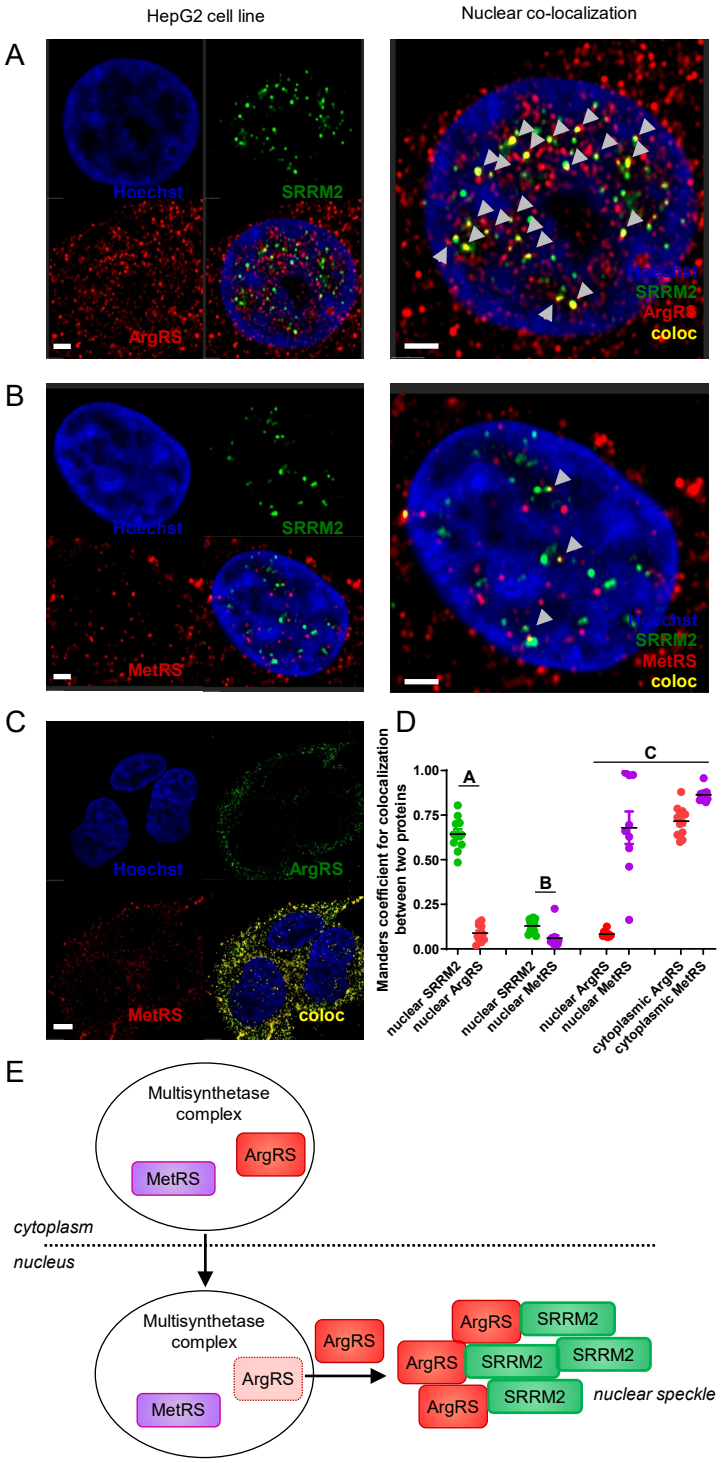
HepG2 cell line
Nuclear co-localization
A
Hoechst
SRRM2
ArgRS
coloc
B
MetRS
C
D
Manders coefficient for colocalization between two proteins
1.00
0.75
0.50
0.25
0.00
nuclear SRRM2
nuclear ArgRS
nuclear SRRM2
nuclear MetRS
nuclear ArgRS
nuclear MetRS
cytoplasmic ArgRS
cytoplasmic MetRS
E
Multisynthetase complex
ArgRS
MetRS
cytoplasm
nucleus
nuclear speckle

Figure 4

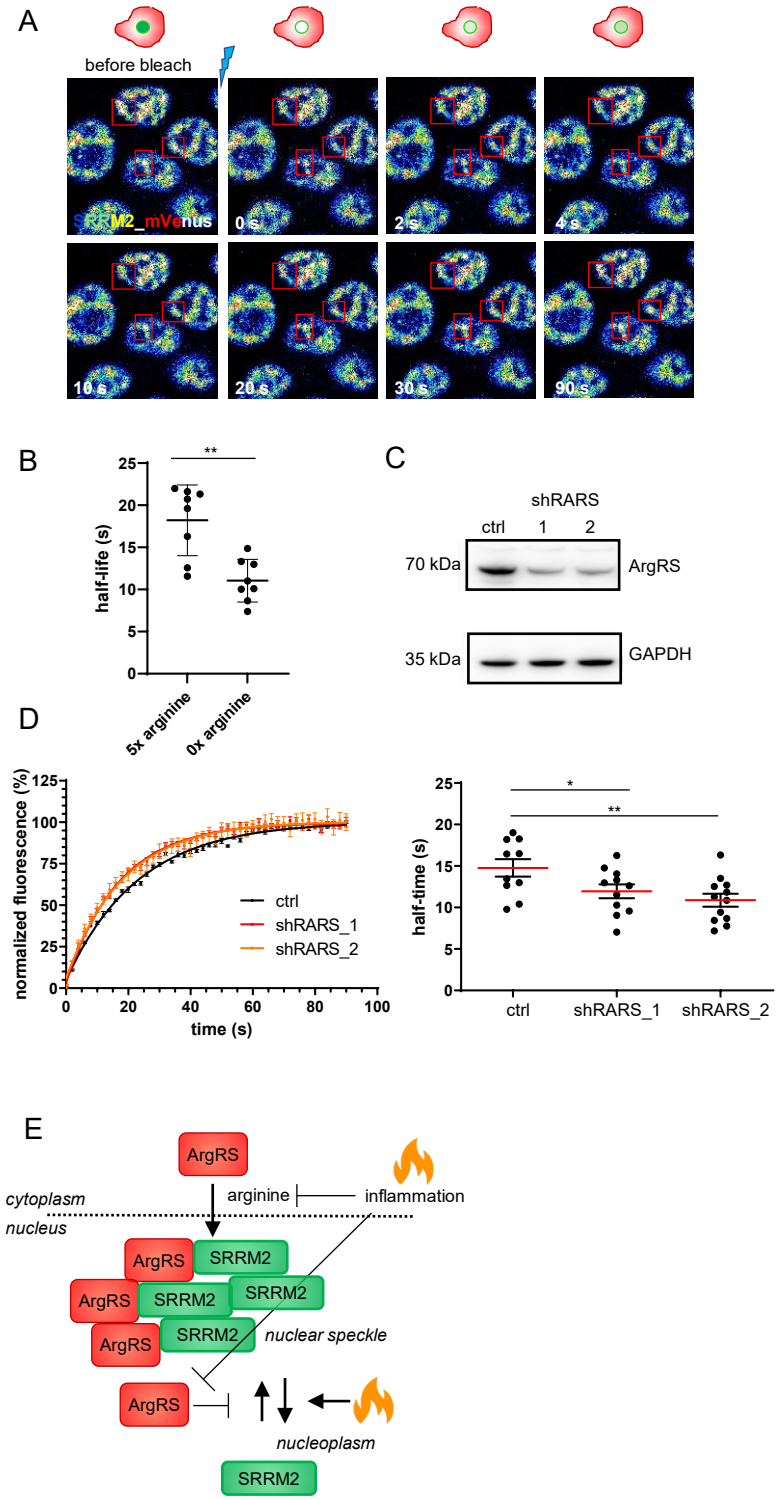
A
before bleach
SRRM2_mVenus
0 s
2 s
4 s
10 s
20 s
30 s
90 s
B
half-life (s)
5x arginine
0x arginine
C
shRARS
ctrl
1
2
70 kDa
ArgRS
35 kDa
GAPDH
D
normalized fluorescence (%)
time (s)
ctrl
shRARS_1
shRARS_2
half-time (s)
E
ArgRS
arginine
inflammation
cytoplasm
nucleus
SRRM2
nuclear speckle
nucleoplasm

Figure 5

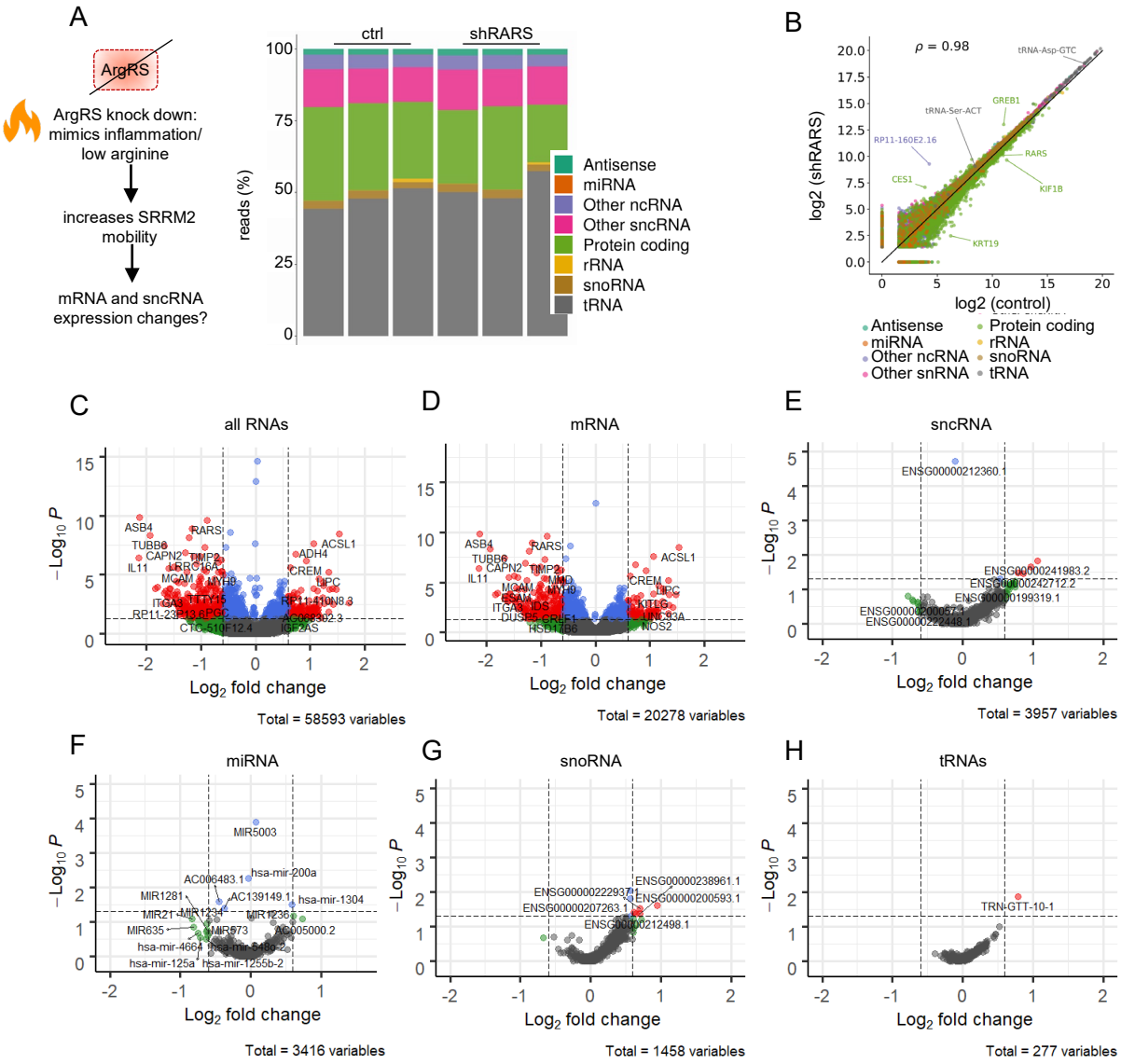
A
ArgRS
ArgRS knock down: mimics inflammation/ low arginine
increases SRRM2 mobility
mRNA and sncRNA expression changes?
ctrl
shRARS
reads (%)
Antisense
miRNA
Other ncRNA
Other sncRNA
Protein coding
rRNA
snoRNA
tRNA
B
ρ = 0.98
log2 (shRARS)
log2 (control)
tRNA-Asp-GTC
GREB1
tRNA-Ser-ACT
RP11-160E2.16
RARS
CES1
KIF1B
KRT19
C
all RNAs
Total = 58593 variables
D
mRNA
Total = 20278 variables
E
sncRNA
Total = 3957 variables
F
miRNA
Total = 3416 variables
G
snoRNA
Total = 1458 variables
H
tRNAs
Total = 277 variables
Log2 fold change
−Log10 P

Figure 6

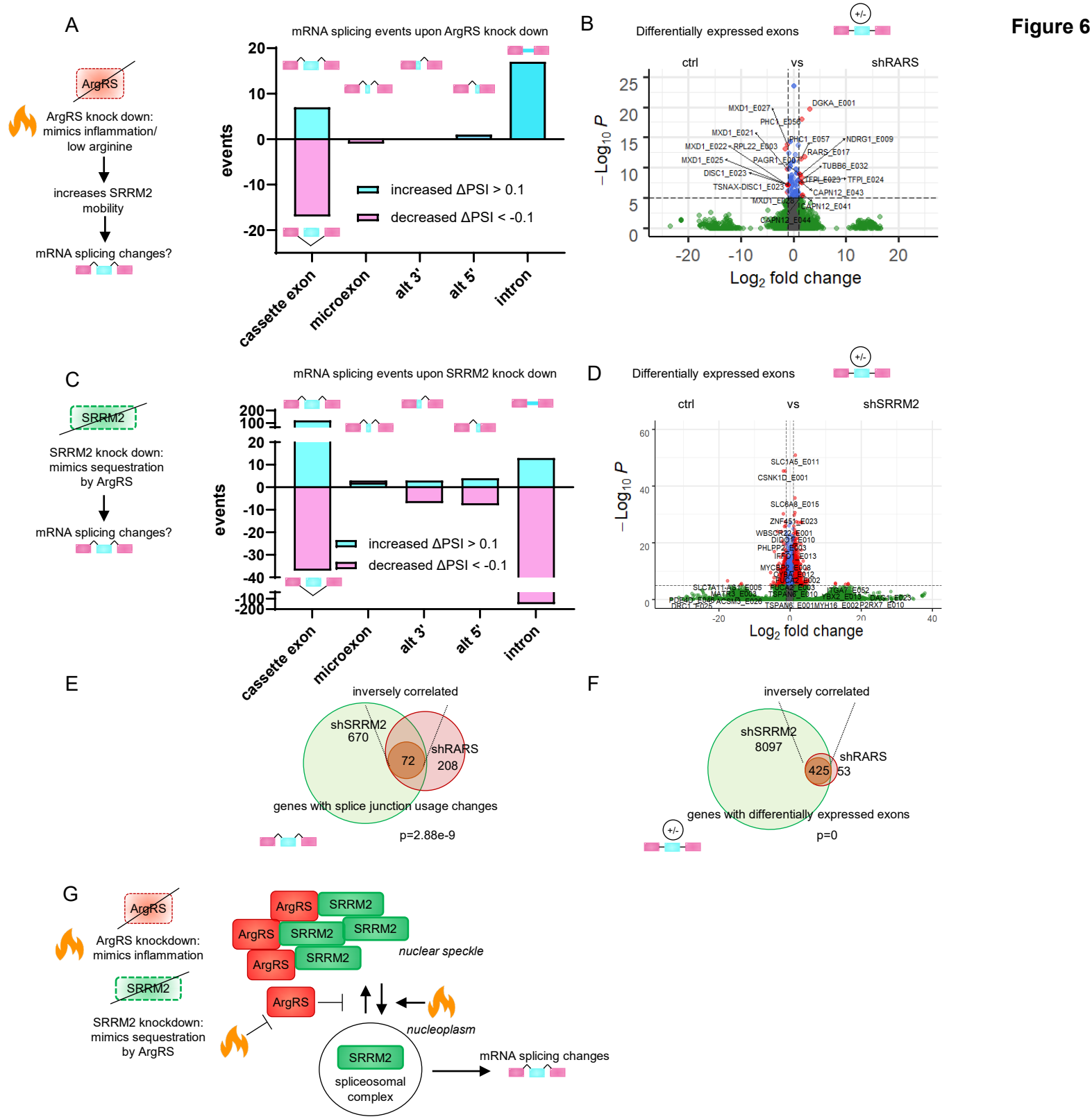
A
ArgRS
ArgRS knock down:
mimics inflammation/
low arginine
increases SRRM2
mobility
mRNA splicing changes?
mRNA splicing events upon ArgRS knock down
events
increased ΔPSI > 0.1
decreased ΔPSI < -0.1
cassette exon
microexon
alt 3'
alt 5'
intron
B
Differentially expressed exons
ctrl
vs
shRARS
−Log10 P
Log2 fold change
C
SRRM2
SRRM2 knock down:
mimics sequestration
by ArgRS
mRNA splicing changes?
mRNA splicing events upon SRRM2 knock down
events
increased ΔPSI > 0.1
decreased ΔPSI < -0.1
cassette exon
microexon
alt 3'
alt 5'
intron
D
Differentially expressed exons
ctrl
vs
shSRRM2
−Log10 P
Log2 fold change
E
inversely correlated
shSRRM2
670
72
shRARS
208
genes with splice junction usage changes
p=2.88e-9
F
inversely correlated
shSRRM2
8097
425
shRARS
53
genes with differentially expressed exons
p=0
G
ArgRS
ArgRS knockdown:
mimics inflammation
SRRM2
SRRM2 knockdown:
mimics sequestration
by ArgRS
ArgRS
SRRM2
nuclear speckle
nucleoplasm
SRRM2
spliceosomal
complex
mRNA splicing changes

Figure 7

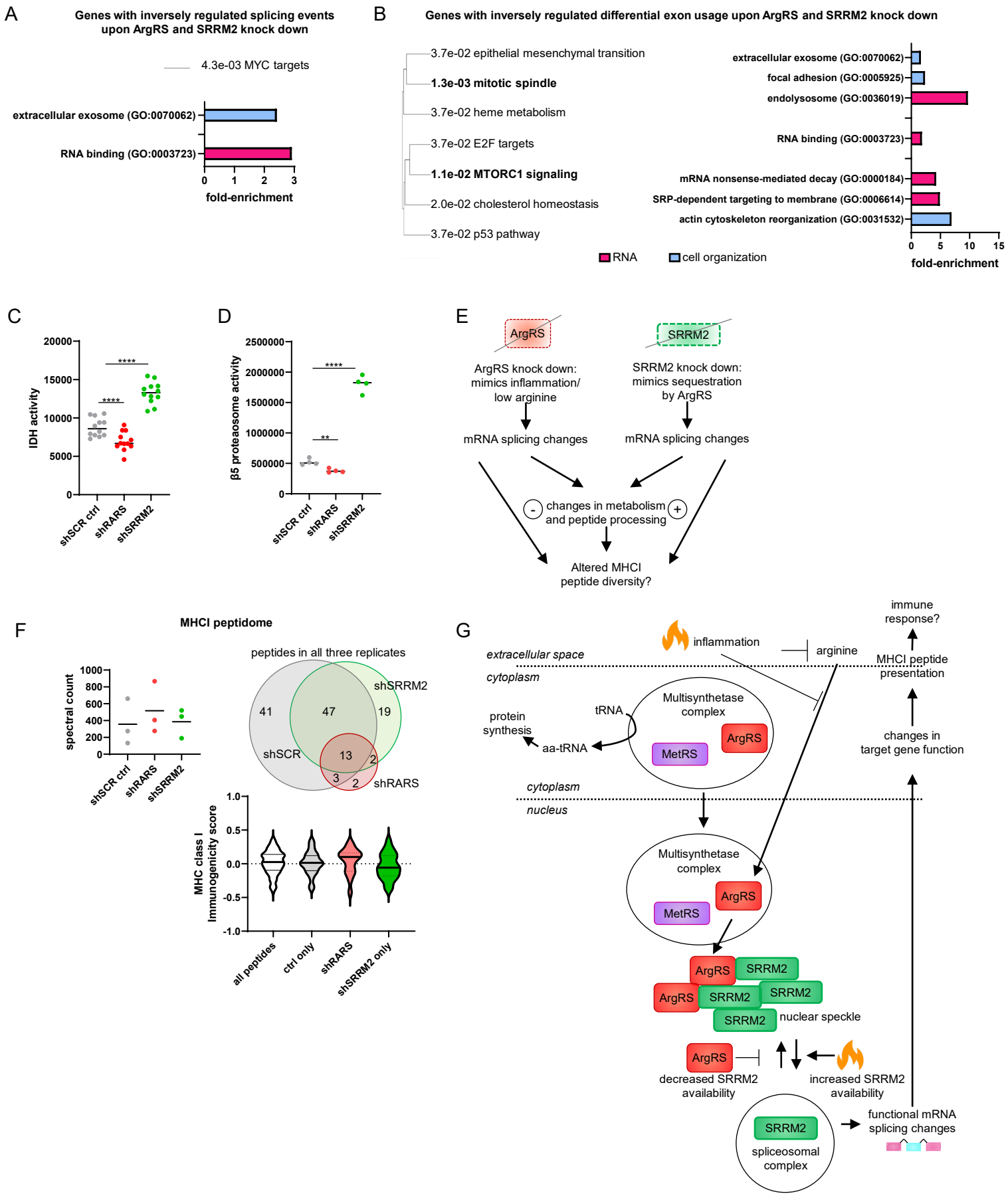
A
Genes with inversely regulated splicing events upon ArgRS and SRRM2 knock down
4.3e-03 MYC targets
extracellular exosome (GO:0070062)
RNA binding (GO:0003723)
0 1 2 3
fold-enrichment
B
Genes with inversely regulated differential exon usage upon ArgRS and SRRM2 knock down
3.7e-02 epithelial mesenchymal transition
1.3e-03 mitotic spindle
3.7e-02 heme metabolism
3.7e-02 E2F targets
1.1e-02 MTORC1 signaling
2.0e-02 cholesterol homeostasis
3.7e-02 p53 pathway
extracellular exosome (GO:0070062)
focal adhesion (GO:0005925)
endolysosome (GO:0036019)
RNA binding (GO:0003723)
mRNA nonsense-mediated decay (GO:0000184)
SRP-dependent targeting to membrane (GO:0006614)
actin cytoskeleton reorganization (GO:0031532)
0 5 10 15
fold-enrichment
RNA
cell organization
C
IDH activity
20000
15000
10000
5000
0
****
****
shSCR ctrl
shRARS
shSRRM2
D
β5 proteaosome activity
2500000
2000000
1500000
1000000
500000
0
****
**
shSCR ctrl
shRARS
shSRRM2
E
ArgRS
SRRM2
ArgRS knock down: mimics inflammation/ low arginine
SRRM2 knock down: mimics sequestration by ArgRS
mRNA splicing changes
mRNA splicing changes
changes in metabolism and peptide processing
Altered MHCI peptide diversity?
F
MHCI peptidome
spectral count
1000
800
600
400
200
0
shSCR ctrl
shRARS
shSRRM2
peptides in all three replicates
shSRRM2
41
47
19
shSCR
13
2
3
2
shRARS
MHC class I Immunogenicity score
1.0
0.5
0.0
-0.5
-1.0
all peptides
ctrl only
shRARS
shSRRM2 only
G
extracellular space
cytoplasm
inflammation
arginine
immune response?
MHCI peptide presentation
protein synthesis
tRNA
aa-tRNA
Multisynthetase complex
ArgRS
MetRS
changes in target gene function
cytoplasm
nucleus
Multisynthetase complex
ArgRS
MetRS
ArgRS
SRRM2
ArgRS
SRRM2
SRRM2
SRRM2
nuclear speckle
ArgRS
decreased SRRM2 availability
increased SRRM2 availability
SRRM2
spliceosomal complex
functional mRNA splicing changes

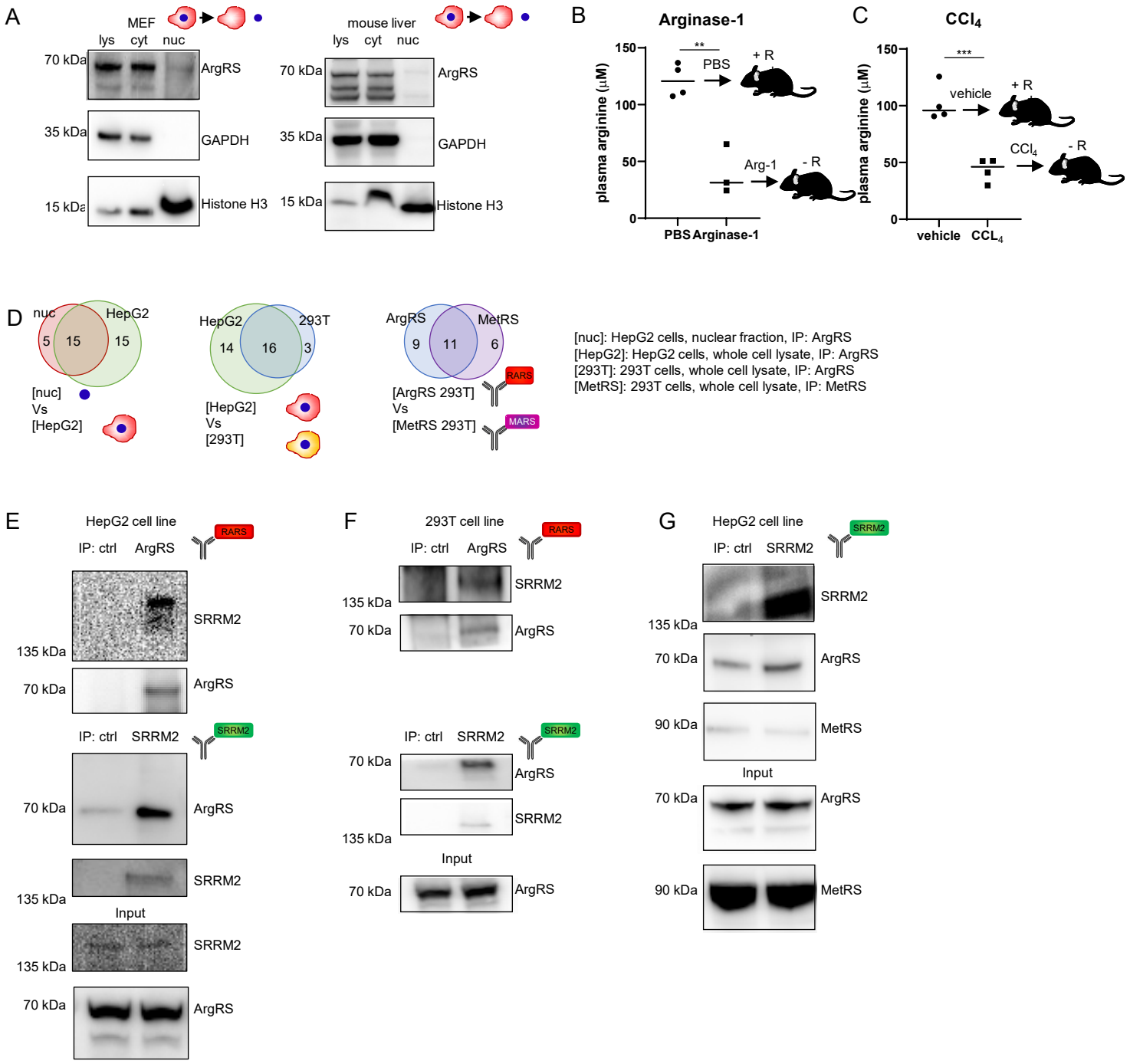

Supplementary Figure 1: ArgRS localizes to the nucleus in murine cells and tissues, plasma arginine levels, and characterization of the ArgRS interactome. (A) ArgRS in different cellular compartments of murine embryonic fibroblasts (MEF, left) and mouse liver (right) probed by western blot following cell fractionation. GAPDH: cytoplasmic marker, Histone H3: nuclear marker. lys: lysate, cyt: cytoplasm, nuc: nucleus. (B, C) LC/MS measurement of plasma arginine after (B) treatment with recombinant Arginase-1, an arginine-degrading enzyme, or (C) by induction of systemic inflammation with the liver toxin CCl_4. n=3 or 4 mice in each group. p= **0.002, p= *** p= 0.0009. (D) Venn diagrams comparing 4 different ArgRS interactomes. Statistical significance of overrepresentation by hypergeometric test: [nuc] vs [HepG2]: p=7.6e-10, [HepG2] vs [293T]: p=1.9e-10, [ArgRS 293T] vs [MetRS 293T]: p=2.0e-7. (E, F) SRRM2 interaction with ArgRS was verified by immunoprecipitation (IP) of ArgRS and vice versa. Detection of ArgRS and SRRM2 by western blot. Ctrl: Non-targeting antibody of the same isotype. (E) Input: HepG2 cell lysate. (F) Input: HEK 293T cell lysate. (G) SRRM2 immunoprecipitation did not retrieve MetRS but ArgRS. Detection of ArgRS, MetRS, and SRRM2 by western blot.

Supplementary Figure S2

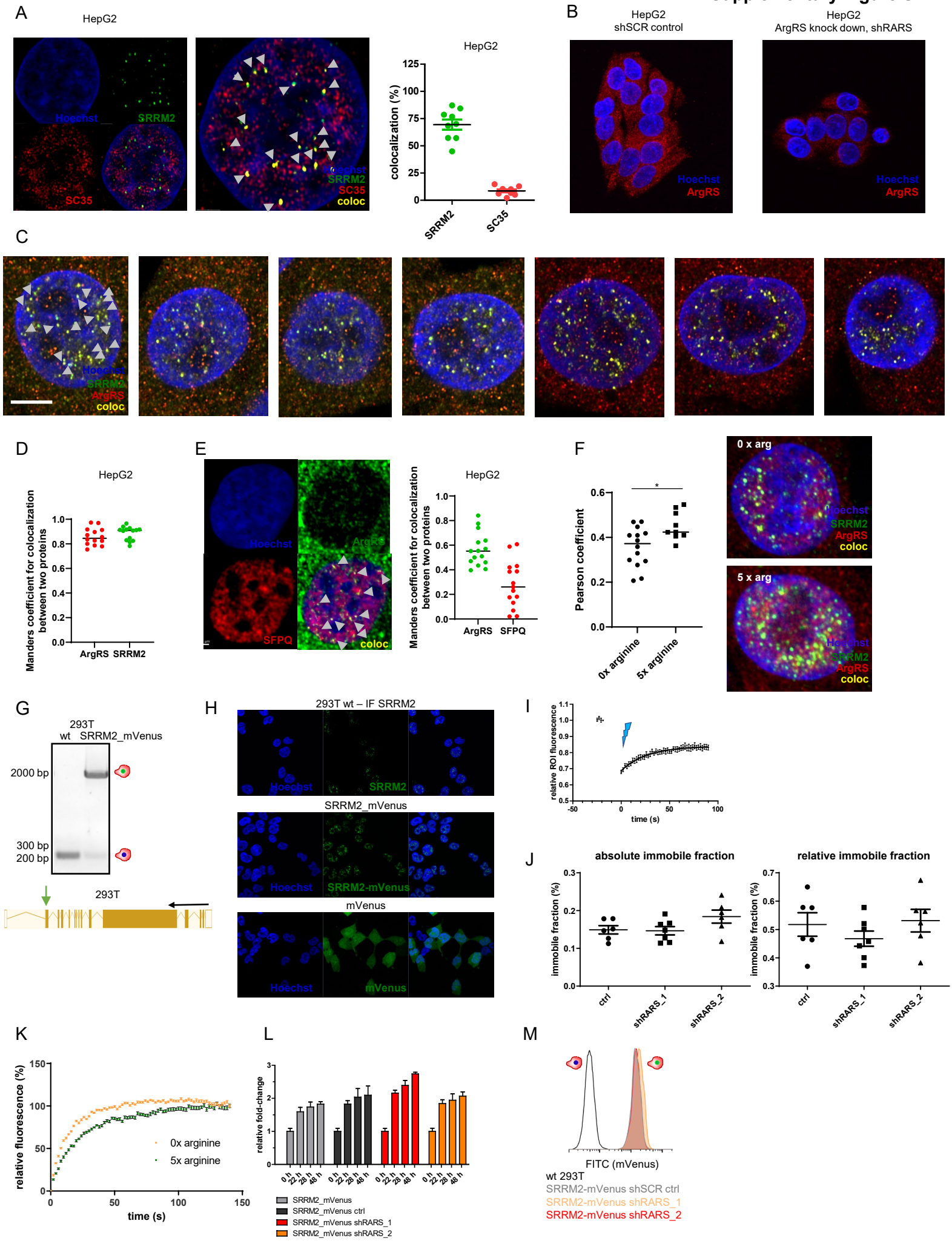

Supplementary Figure 2: Fluorescent microscopy to assess SRRM2 colocalization and dynamics. (A) Colocalization (yellow) of SRRM2 (green) and speckle marker SC35 (red) by immunofluorescent staining and imaging by confocal microscopy. Close to 75% of all SRRM2 colocalized with SC35. (B) Maximum intensity projections of ArgRS immunofluorescent staining in HepG2 shSCR control and shRARS_1 cells to show antibody specificity. (C) Immunofluorescent staining of ArgRS and SRRM2 in representative nuclei. Bar: 5 µm. (D) Manders coefficient of ArgRS and SRRM2 colocalization when Costes thresholding was used. (E) Colocalization of ArgRS (green) and paraspeckle protein SFPQ (red). Manders coefficient of colocalization after Costes thresholding. (F) Pearson correlation coefficient of SRRM2 and ArgRS colocalization by immunofluorescence staining upon arginine starvation (0x arginine) and high arginine (5x arginine). Representative immunofluorescent staining of ArgRS and SRRM2. p=*0.01, n=14, 9. Arginine concentration relative to DMEM. (G) Labeling of endogenous SRRM2 with the fluorescent protein mVenus. Verification of genomic mVenus insertion by PCR. Predicted amplification length of wildtype amplicon: 238 bp; predicted length of SRRM2-mVenus amplicon: 2071 bp. (H) Labeling with mVenus did not alter SRRM2 localization in 293T cells. Endogenous, unlabeled SRRM2 was visualized by immunofluorescence (upper panel). SRRM2-mVenus fluorescence displayed a similar pattern with fluorescence restricted to the cell nucleus and defined foci (middle panel). In comparison, stable expression of mVenus alone did not display a distinct localization (lower panel). (I) Fluorescence Recovery After Photobleaching (FRAP) measured over 90 s. Recovery reached its plateau after 60 s. (J) Absolute immobile SRRM2-mVenus fraction calculated from one-exponential curve fits of FRAP measurements and relative immobile fraction calculated by subtraction of residual fluorescence directly after bleaching. (K) Recovery of fluorescent signal is faster in the absence of arginine. Fluorescent signal was corrected for background and normalized. Each measurement included 14 regions of interest and the geometric mean of 8 measurements is shown. Errors bars depict standard error of the mean. (L) Cell viability upon ArgRS knock down in SRRM2-mVenus cells, measured with Alamar Blue. Technical quadruplets are shown. (M) Knock down of ArgRS did not affect SRRM2-mVenus protein levels measured by flow cytometry.

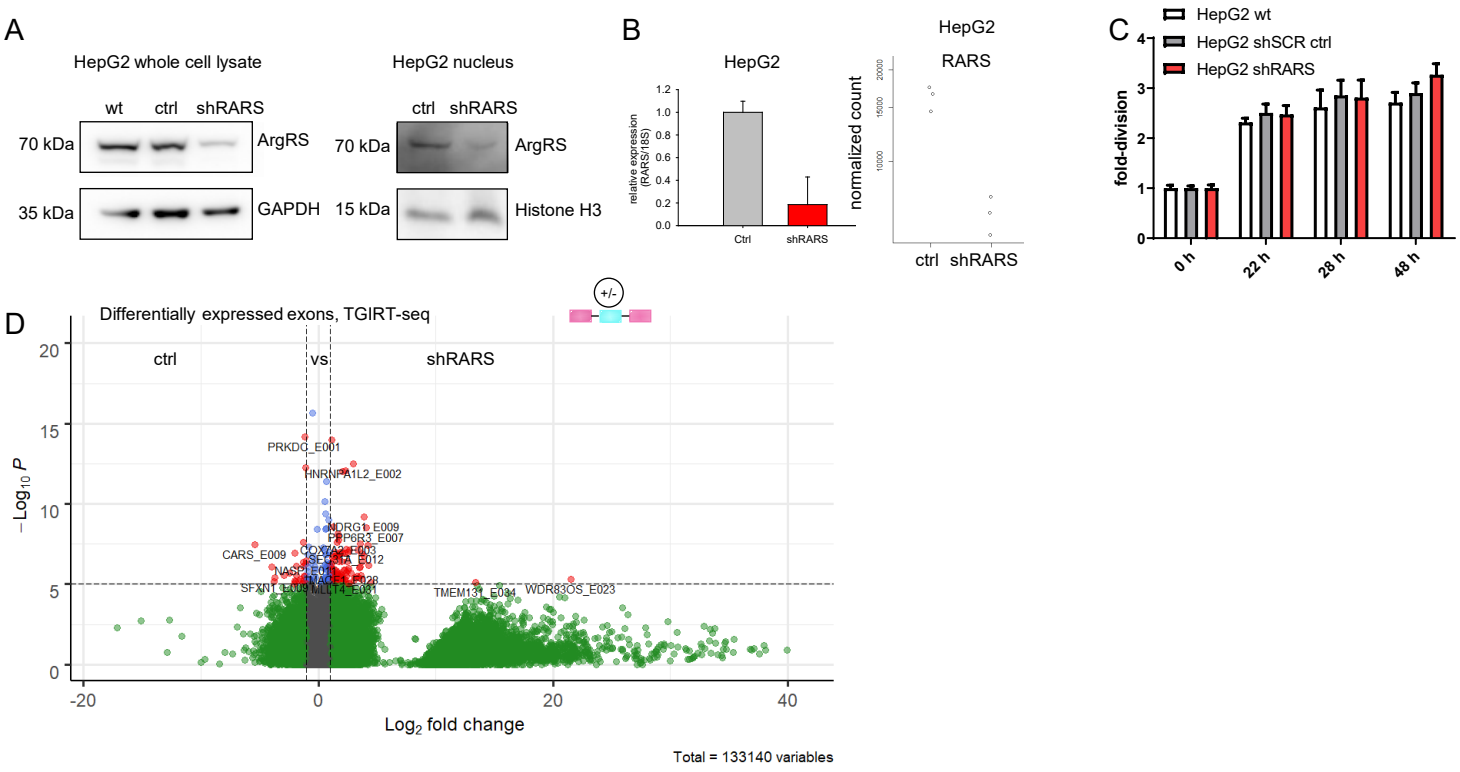

Supplementary Figure 3: Characterization of ArgRS knock down. (A) ArgRS knock down was confirmed on protein level by western blot and (B) on mRNA level by RT-qPCR and RNA-seq. A representative out of 3 repeats is shown. (C) Cell viability and proliferation of HepG2 cells was not affected by ArgRS knock down. Alamar blue based cell viability assay, quadruplets of technical replicates are shown. (D) Volcano plot of differentially expressed exons upon ArgRS knock down as found by TGIRT-seq. Dashed vertical lines: 2-fold change, dashed horizontal line: p-value 1e-6. (A-D) ctrl: shSCR control, shRARS: ArgRS knock down.

Supplementary Figure S4

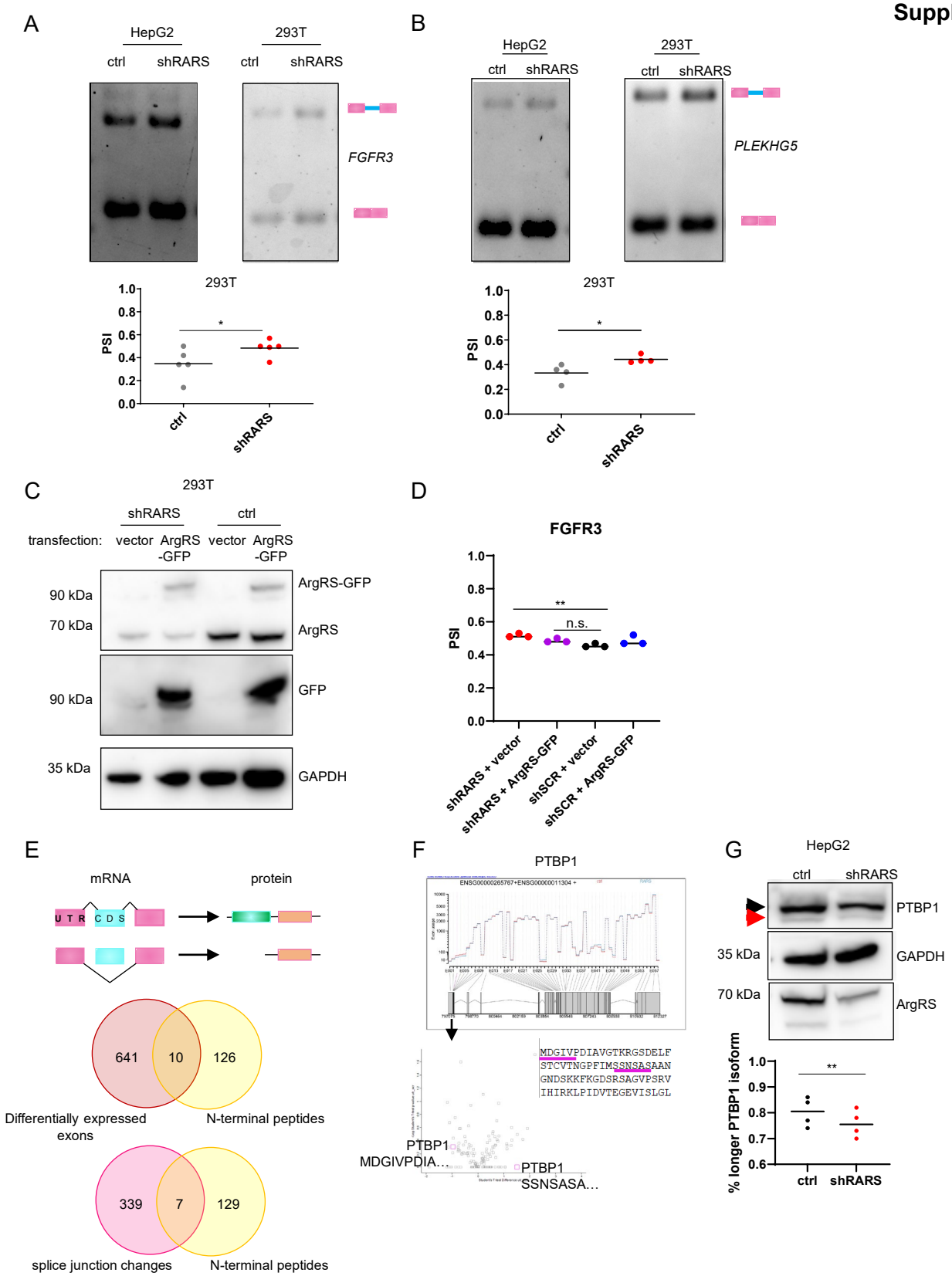

Supplementary Figure 4: ArgRS knock down affected mRNA processing and protein isoforms. (A, B) RT-PCR of splice isoforms for (A) *FGFR3* and (B) *PLEKHG5*. Genes were detected as alternatively spliced in HepG2 cells by RNA-seq and confirmed for HEK 293T cells. A representative image from 3 or more replicates is shown as well as the densitometric quantification for 293T. PSI: percent spliced in. Ctrl: shSCR control. p=*0.001, n=5, 5. p= *0.03, n=4, 4. (C) Rescue of ArgRS knock down by overexpression of ArgRS-GFP by transient transfection in 293T cells, shown by western blot. (D) Rescue of *FGFR3* splicing by overexpression of ArgRS-GFP. Densitometric analysis of 3 repeats is shown. p= *0.003, n=3, 3, 3, 3. (E) Genes and their corresponding proteins shared between differentially expressed exons or splice junction changes (RNA-seq) and N-terminal peptides (proteomics) in ArgRS knock down vs control cells. (F) Peptides found for PTBP1 in mass spectrometry following the enrichment of N-terminal peptides. (G) Western blot verification of preference for a higher molecular weight form of PTBP1 after ArgRS knock down. p=*0.003, n=4, 4.

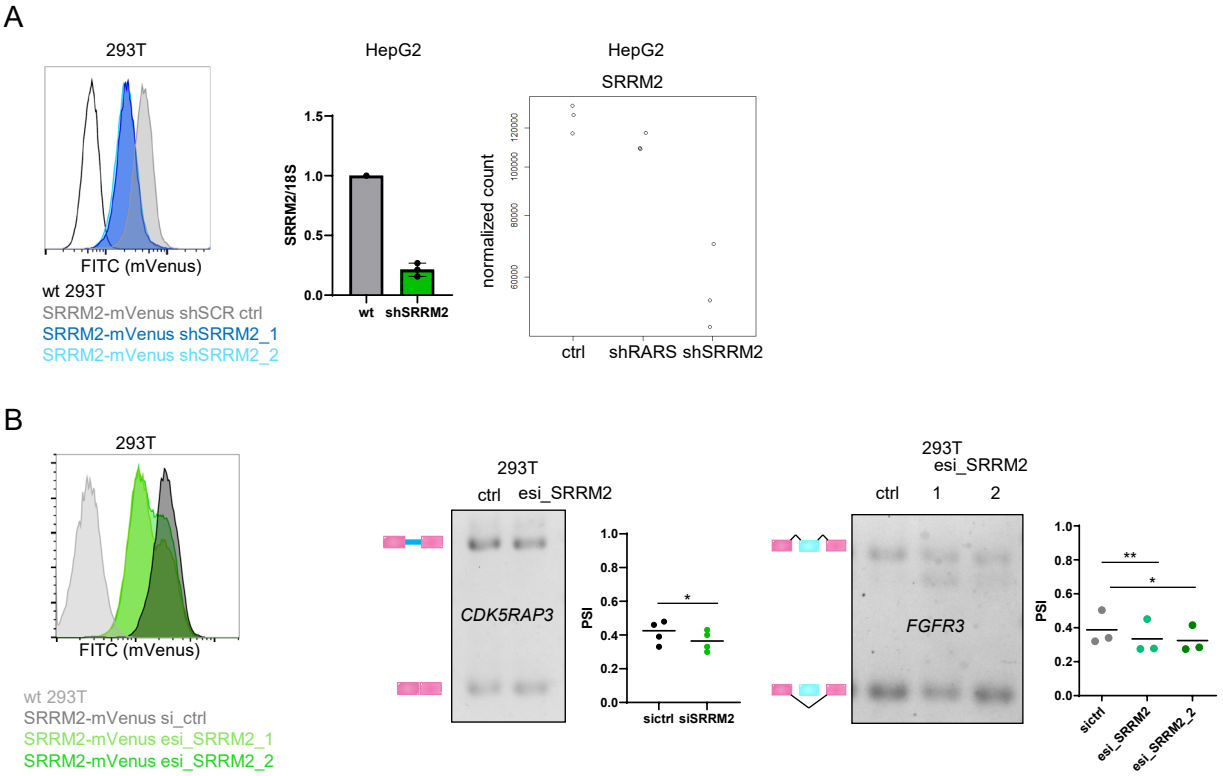

Supplementary Figure 5: Verification of stable and transient SRRM2 knock down and its effects on mRNA splicing. (A) Left to right: Knock down of SRRM2 in 293T_SRRM2_mVenus cells to verify shRNAs later used in HepG2 cells, assessed by flow cytometry. < 50% medium fluorescence intensity reduction upon SRRM2 knock down. Knock down of SRRM2 in HepG2 verified by qRT-PCR, three repeats, each measured in triplicates. Normalized SRRM2 counts in RNAseq. (B) Left: Verification of transient SRRM2 knock down by a heterogenous pool of siRNAs (esiRNA) in 293T_mVenus cells using flow cytometry. esi_SRRM2 1 and 2 are different batches of the same pool. ctrl: non-targeting pool of siRNAs. Right: RT-PCR splicing assays of *CDK5RAP3* and *FGFR3* upon transient knock down of SRRM2 with a pool of esiRNA in 293T cells. *CDK5RAP3*: p= *0.03, n=4, 4. *FGFR3:* p = **0.01, *0.04, n=3, 3, 3.

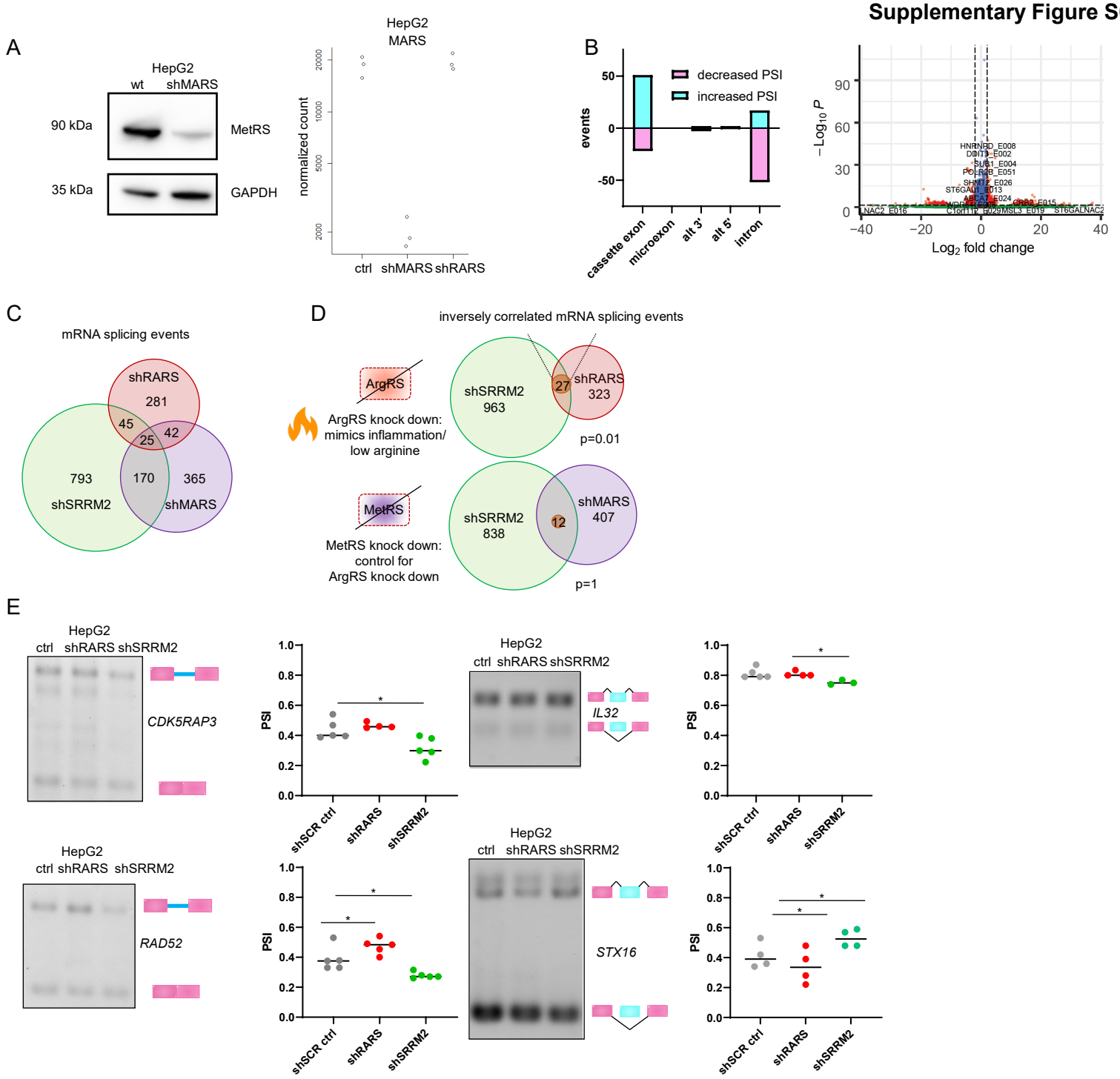

Supplementary Figure 6: Characterization of MetRS knock down and verification of splicing events regulated by ArgRS and SRRM2 in opposite directions. (A) Verification of MetRS knock down (shMARS) by western blot and RNAseq. (B) Splicing events with |ΔPSI| > 0.1, MV > 0 and differential exon usage (padj < 0.05). Dashed vertical lines: 2-fold change, dashed horizontal line: 1e-6. (C) Venn diagram of shared splicing event changes upon knock down of ArgRS, SRRM2, or MetRS. All splicing event changes relative to shSCR control. MV > 0, no criterion for |ΔPSI|. (D) Inversely correlated alternative splicing events shared between ArgRS and SRRM2 or MetRS and SRRM2. Hypergeometric test for overrepresentation. (E) Knock down of ArgRS and SRRM2 had opposite effects on *CDK5RAP3*, *RAD52*, and *STX16* processing as shown by RT-PCR. Representatives of 4 or 5 replicates shown with quantification by densitometry. Scheme of SRRM2 sequestration by ArgRS and resulting altered mRNA splicing. *CDK5RAP3*: p = *0.02, n= 5, 4, 5. *IL32*: p=*0.03, n=4, 4, 3. *RAD52*: p= *0.02, *0.04, n= 5, 5, 5. *STX16*: p= *0.04, *0.04, n=4, 4, 4.

Supplementary Figure S7

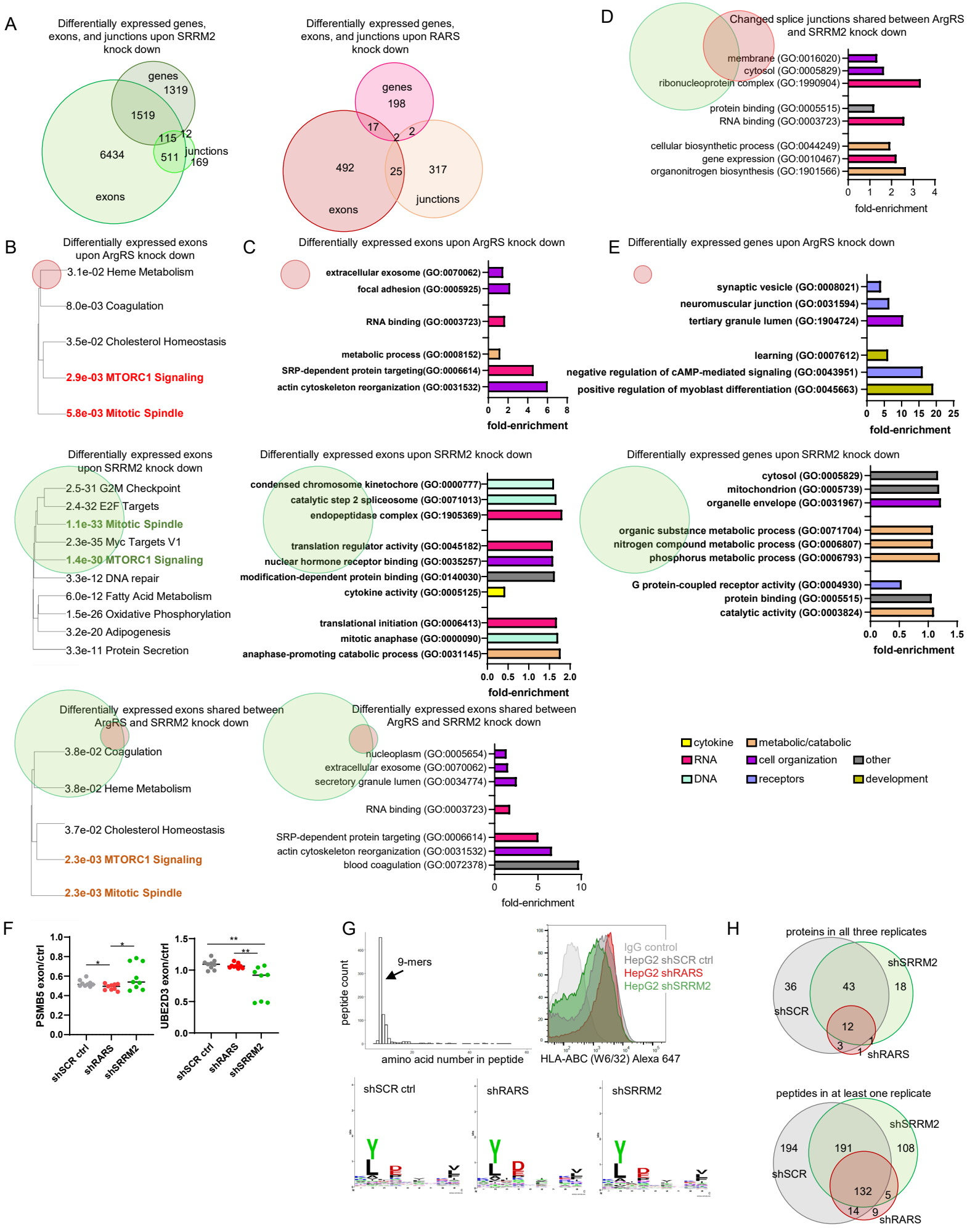

Supplementary Figure 7: SRRM2 and ArgRS induced changes and their effects on cellular signaling. (A) Comparison of genes with differential gene expression, differential exons, and splice junctions for shSRRM2 and shRARS. (B) Genes with differentially expressed exons enriched in MSigDB hallmark categories upon SRRM2 and ArgRS knock down (padj < 0.05) in HepG2. (C) Gene Ontology (GO) enrichment of genes with differentially expressed exons upon SRRM2 and ArgRS knock down (padj < 0.05) in HepG2. (D) GO enrichment of genes with changed splice junctions upon SRRM2 and ArgRS knock down (MV > 0) in HepG2. (C, D) All expressed genes were used as reference. (E) MSigDB hallmark categories and GO enrichment of genes with differential gene expression shared between SRRM2 and ArgRS knock down. (B-E) Circle size and Venn diagram visualize the proportion of shared exons, junctions, or genes. (F) Quantification of differentially expressed exons by qRT-PCR. PSMB5: p= *0.03, *0.04. UBE2D3: p=**0.006, **0.008. (G) (top left) Length distribution histogram of MHCI peptides confirmed that isolated peptides consisted predominantly of 9 amino acid peptides. (top right) Flow cytometry of MHCI on HepG2 shSCR ctrl, ArgRS knock down, and SRRM2 knock down cells by antibody staining. (bottom). Comparable overrepresentation of amino acids at specific positions (2, 4) were found with WebLogo in 9 amino acid-long peptides. (H) Venn diagrams of identified MHCI peptides by mass spectrometry following isolation of MHCI complex, displayed as proteins corresponding to the detected peptides found in all replicates (upper panel) and peptides found in at least one replicate (lower panel).